6

Some Features of The Volume Component of Radar Backscatter From Thick and Dry Snow Cover

Boris Yurchak
University of Maryland, Baltimore County, GEST
USA

1. Introduction

Radar monitoring of thick snow cover in polar regions with optical thickness (a product of the depth of the snow and the extinction coefficient) of order 1 or more from elevated above-ground and space platforms is of great importance for registration and for understanding glaciology processes caused by climatic change. Applicable to this issue, the volume component of the backscatter coefficient has a notable contribution to the total backscatter (Noveltis, 2005). Although the idea of the radar-cross section (RCS) term and its derivatives, like the backscatter coefficient, aims to separate as far as possible the sensor (radar) and target parameters, this distinction can rarely be fulfilled in the case of spatially extended geophysical targets (SEGT), such as atmospheric clouds and rain, as well as the thick snow cover that is the focus of this paper. Due to this feature, the analysis of backscatter from SEGT strongly depends on the relationship between the technical and physical-geometrical properties of the radar and target, respectively. The main parameters that govern the radar-target configuration for snow sounding are wavelength, antenna characteristics, pulse duration, sounding direction, extinction coefficient and the geometrical depth of the snow. A correct assessment of the volume component of the backscatter coefficient and an understanding of the realm of applicability of any backscattering model is possible only when the size of the scattering volume within a snow slab is known. This parameter depends on the factors mentioned above and should be distinguished for different situations in the practice of radar sounding of snow-covered terrain by Synthetic Aperture Radar (SAR), a scatterometer or an altimeter. This work attempts, at first, to determine the radar-target configurations inherent to volume scattering estimations of the thick snow cover under the different radar applications mentioned above. Next, we analyze the range of applications of the incoherent approach for backscatter magnitude estimation, currently one of the main techniques for snow characteristics assessment. The simplest incoherent approach, based on the so-called "particle" or "discrete" approximation, leads to the dependence of backscatter on the sixth moment of the particle size distribution function (PSDF) and the mean amount of particles in the scattering volume (Siegert & Goldstein, 1951; Battan, 1959; Ulaby et al., 1982). For a medium with losses (such as a thick snow slab) the modification of this approach is referred to as the semi-empirical model (Attema &

Ulaby, 1978; Ulaby et al., 1982; Ulaby et al., 1996). There is some evidence of less backscatter occurring than expected by virtue of the conventional reflectivity factor and the backscatter coefficient for incoherent scatter from homogeneous thick snow slab (e.g., Rott et al., 1993). For dense media (mean distance between particles is less than the wavelength) there are many references in the literature that the backscatter is determined by media inhomogeneities (Naito & Atlas, 1967; Gossard & Srauch, 1983; Fung, 1994). To attempt to evaluate the contributions of these inhomogeneities, the radiative transfer (RT) and the dense media radiative transfer (DMRT) models were developed (e.g., Ulaby et al., 1982; Fung, 1994; Tsang et al., 2007). A review of these models and their modifications provided by Noveltis (2005) stated that in certain aspects, these approaches showed some successes. However, these models have not the close-form solutions that make difficult to use them and analyze results obtained. Kendra et al. (1998), based on experiments with artificial snow of varying depths, concluded that both conventional and dense-medium radiative transfer models fail to adequately explain the observed results.

Finding an appropriate and relatively simple approach to calculate the volume component of backscatter to explain the observable deviations from the classical (incoherent) model is therefore a relevant task. The majority of previous studies, focusing on measurements of a dry snow at temperate latitudes, where the snow depth seldom exceeds 1 m and the corresponding optical thickness is much less than 1, have led to the conclusion that such an approach is not feasible because of the much weaker interaction of the electromagnetic radiation of radar wavebands with ice particles within the snow compared with the backscatter from the soil beneath. The current study focuses on the case of the Greenland ice sheet, however, where the depth of snow significantly exceeds that found in temperate latitudes. This favorable condition, in conjunction with the recent finding that the incoherent approach is only a specific case of a more comprehensive description of electromagnetic wave interactions with spatially-extended individual scatterers (Yurchak, 2009), provides a reason for more detailed investigations of the possibilities of the semi-empirical model for interpreting the observable features of radar backscatter from thick snow cover.

2. Condition of complete burial of the probing pulse into snow medium

To estimate the volume component of backscatter from a snow slab, it is first necessary to understand whether the probing pulse is completely buried within the snow slab or whether the illuminated volume is only part of the probing pulse volume. In weather radar meteorology, applicable to rain and clouds, this problem is known as “partial (or incomplete) beam filling,” with a corresponding factor included in the weather radar equation (e.g., Clift, 1985). For sounding thick snow cover, this issue is practically not discussed and is different compared with the sounding of meteorological targets. Complete burial depends on the sounding configuration and snow slab depth. The main criterion for complete burial is the location of the pulse scattering volume with angular size equal to the angular antenna beam width and with spatial length equal to one half of the actual spatial duration of the transmitted pulse into a snow layer. Thus, for complete burial, the angular and radial sizes of the backscatter volume should be matched with the snow slab depth, which is usually known only roughly for a particular geographical region. This condition poses problems for practical applications. Nevertheless, to better understand possible situations where complete burial is feasible, the requirements for the angular antenna beam

size and the probing pulse duration will be analyzed separately for different major sounding configurations.

2.1. Condition of complete burial of the angular (transverse) size of the pulse volume

2.1.1. Oblique sounding, flat surface, plane wavefront

The scheme of this configuration is shown in Figure 2.1. Here, and everywhere below, the snow slab is assumed to have limited depth and an unbounded horizontal extent.

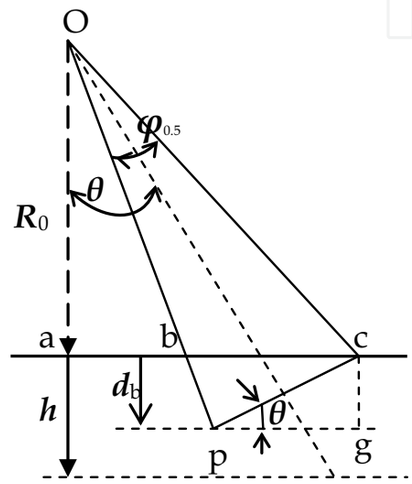

Fig. 2.1. Scheme of sounding for flat surface and plane wavefront

Mathematically, the condition for complete burial in this case is:

$$d_b \le h \tag{2.1}$$

where d_b is the burial depth of the advance point (p) of pulse edge (leading or trailing) when the lagging point (c) reaches the surface and h is the snow depth. As follows from the geometry of Figure 2.1:

$d_b = cg = pc \times \sin\angle cpg$; $\angle cpg = \theta$; $pc \approx 2\frac{R_0}{\cos\theta} tg\frac{\varphi_{0.5}}{2}$, and hence:

$$d_b = 2\frac{R_0}{\cos\theta} tg\frac{\varphi_{0.5}}{2}\sin\theta \tag{2.2}$$

For $\varphi_{0.5}$<<1 one can state $tg\frac{\varphi_{0.5}}{2} \approx \frac{\varphi_{0.5}}{2}$, and condition (2.1) has the form:

$$\varphi_{0.5} \le \frac{h}{R_0}\frac{1}{tg\theta} \tag{2.3}$$

If h~10 m and R_0=800 km, then $\varphi_{0.5} << \frac{1.25}{tg\theta}10^{-5}$ and for θ~40^0, for example, the burial condition (2.1) is satisfied at roughly $\varphi_{0.5}$<<0.001^0. Obviously, this condition can not be fulfilled for any space-based radar system with a real aperture, but it is possible for the SAR if one assumes that the effective synthetic aperture radar beam illuminating an element of spatial resolution Δx on a flat surface can be equal to an extremely narrow, pencil-like beam with $\varphi_{0.5} \sim \frac{\Delta x}{R}$. For example, RadarSAT-1 has Δx ~12.5 m with an orbit height of approximately 800 km and thus, $\varphi_{0.5}$~$0.9*10^{-3}$ degrees. If one assumes that the typical size of the main lobe of the conventional antenna pattern is of order ~1^0, the complete burial of the transverse size of the pulse volume is possible for $\frac{h}{R_0} \geq \varphi_{0.5} tg\theta \sim 2 \cdot 10^{-2} tg\theta$. This condition can definitely be fulfilled for airborne and above-surface elevated radars. The estimate obtained above should be considered only a rough approximation, because at nadir sounding (θ=0) and unbounded horizontal extent of snow slab, the wavefront can not be considered planar for the assessment provided. A more precise estimate is given below.

2.1.2. Oblique sounding, flat surface, spherical wavefront

A real wavefront within a snow slab has a spherical shape. The impact of this shape on the estimation of d_b as the look angle θ (Figure 2.1) decreases begins at the moment when the line tangent to the spherical front at point p coincides with the horizontal line pg, Figure 2.2. This situation takes place when θ becomes equal to the angle between pc and the tangent:

$$\theta = \gamma \tag{2.4}$$

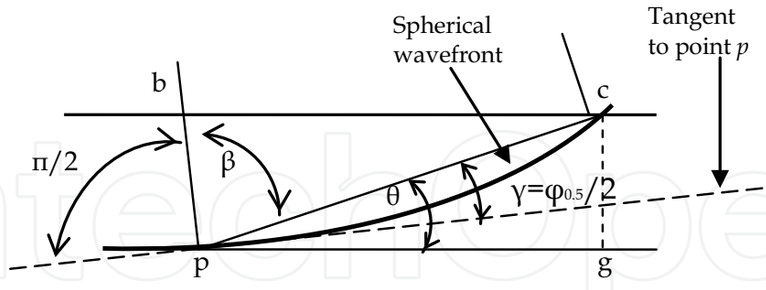

Fig. 2.2. To an assessment of sphericity impact

As follows from geometrical sketch, the auxiliary angle β is equal to: $\beta = \frac{\pi - \varphi_{0.5}}{2}$ and, thus, $\gamma = \frac{\pi}{2} - \beta = \frac{\varphi_{0.5}}{2}$. Therefore, the impact of sphericity should be taken into account only for small look angles, when

$$\theta \le \frac{\varphi_{0.5}}{2} \tag{2.5}$$

Thus, the estimate (2.3), provided in the previous subsection, is valid for $\theta > \frac{\varphi_{0.5}}{2}$. An estimate for configurations close to nadir sounding will be carried out in the next subsection.

2.1.3. Nadir sounding, flat surface spherical wavefront

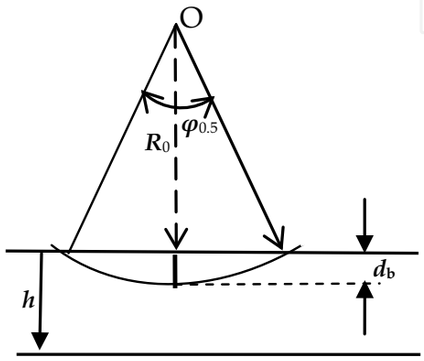

Fig. 2.3. Schematic of sounding in nadir direction

This configuration is shown schematically in Figure 2.3 and the corresponding condition for complete burial is:

$$d_b^{(flt)} \le h \tag{2.6}$$

From the geometrical configuration and $\varphi_{0.5}$<<1, it follows that:

$$d_b^{(flt)} = R_0\left(\frac{1}{\cos\frac{\varphi_{0.5}}{2}} - 1\right) = R_0\frac{2\sin^2\frac{\varphi_{0.5}}{4}}{\cos\frac{\varphi_{0.5}}{2}} \approx \frac{1}{8}R_0\varphi_{0.5}^2 \tag{2.7}$$

This estimate can be accepted for elevated platforms (for example, airborne radars and those mounted above the surface) but needs to be analyzed further for space platforms due to the sphericity of the surface, as the corresponding area illuminated on the Earth's surface by conventional radar is large.

2.1.4. Nadir sounding, spherical surface, spherical wavefront

In the spherical surface approach, the depth of complete burial in altimeter mode is more than that for a flat surface described above by an increment Δz in the center of the beam. This effect is illustrated in Figure 2.4, and can be written as:

$$d_b^{(sp)} = d_b + \Delta z \le h \tag{2.8}$$

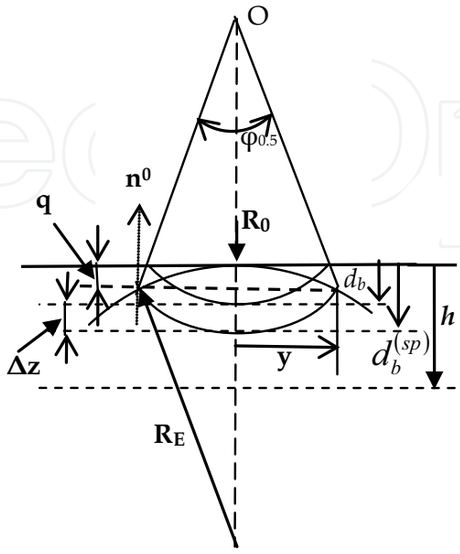

Fig. 2.4. Estimation of complete burial of an increment of pulse due to the sphericity of the Earth

Based on the geometrical relations of the sketch, the following system of equations may be composed

$$\begin{cases} \dfrac{y}{R_0 + q} = tg\dfrac{\varphi_{0.5}}{2} \\ R_E^2 = (R_E - q)^2 + y^2 \end{cases} \tag{2.9}$$

where $q = \Delta z \cdot \cos\dfrac{\varphi_{0.5}}{2}$, and y is the distance between the vertical axis and the beam periphery touching the spherical surface. Solving this system, the increment due to the sphericity is equal to:

$$q = \frac{R_E - R_0 tg^2\dfrac{\varphi_{0.5}}{2}}{\left(1 + tg^2\dfrac{\varphi_{0.5}}{2}\right)}\left[1 \pm \sqrt{1 - \frac{\left(1 + tg^2\dfrac{\varphi_{0.5}}{2}\right)\left(R_0 tg\dfrac{\varphi_{0.5}}{2}\right)^2}{\left(R_E - R_0 tg^2\dfrac{\varphi_{0.5}}{2}\right)^2}}\right] \tag{2.10}$$

where R_E is the Earth's radius. Taking into account that $\dfrac{\varphi_{0.5}}{2} << 1$, $\dfrac{R_E}{R_0} > 1$, and that the minus sign should be taken before the square root for physical reasons, the above formulae

can be simplified significantly, yielding an increment equal to:

$$\Delta z \approx \frac{1}{2}\frac{R_0}{R_E}R_0\left(\frac{\varphi_{0.5}}{2}\right)^2\left(\cos\frac{\varphi_{0.5}}{2}\right)^{-1} \tag{2.11}$$

A numerical assessment under the parameters values listed above gives Δz~5 m. The estimation of the parameter $d_b^{(sp)}$ can be represented in the form:

$$d_b^{(sp)} = R_0\left(\frac{1}{\cos\frac{\varphi_{0.5}}{2}}-1\right)+\frac{1}{2}\frac{R_0}{R_E}R_0\left(\frac{\varphi_{0.5}}{2}\right)^2\frac{1}{\cos\frac{\varphi_{0.5}}{2}} \approx \frac{1}{8}R_0\varphi_{0.5}^2\left(1+\frac{R_0}{R_E}\right) \tag{2.12}$$

This relationship coincides with the estimate obtained by Barrick (1972) for a spherical wave increment over the spherical mean sea surface. For R_0=800 km, R_E=6400 km and $\varphi_{0.5}=1^0$, one calculates $d_b^{(sp)}$≈45 m. This result means that the Earth's sphericity increases the complete burial parameter compared with the flat surface case (see 2.7) by a factor of ~$(1+\frac{R_0}{R_E})$. For $\frac{R_0}{R_E}\approx\frac{1}{8}$ the complete burial parameter equals to 1.125, i.e., a 12.5% increase.

Based on known assessments of penetration depth of 2-5 m for Ku-band (e.g., Davis, 1996), the wave sphericity in practice does not allow for consideration of the complete burial of the transversal size of the probing pulse for a space-based altimeter and scatterometer. This sphericity causes the area illuminated on the surface to change as the probing pulse is buried into a snow slab. It can be easily shown that the radius of the illuminated area changes with the burial increment ΔR as $r_{ill} \approx \sqrt{2R_0 \cdot \Delta R}$.

2.1.5. Wavefront flattening

The speed of an electromagnetic wave within a snow slab is lower than that in an air by $\sqrt{\varepsilon'}$, where ε′ is the real part of the dielectric permittivity of snow. For dry snow within a density range of 0.2-0.5 g/cm³, parameter ε′ changes roughly from 1.35 to 1.95 (Tiuri et al., 1984). Recently, a decrease in wave speed was also confirmed by direct measurements in snow (Scott et al., 2006). Due to the sphericities of the Earth and the wavefront, the paths of the wave for different rays into a snow slab for equal time are not the same that results from the distortion of the initial spherical wave front, as demonstrated in Figure 2.5.

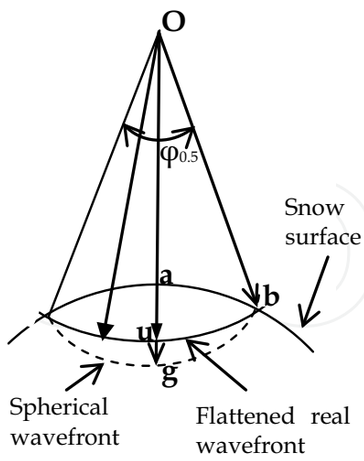

Fig. 2.5. Illustration of the flattening of a spherical wavefront within a snow slab

The peripheral ray (ray *Ob*, for example) has a different path into a snow slab as compared with the central ray (*Og*), which that has a portion *ag* extending into the snow. This feature causes the flattening of the spherical wavefront. Thus, the snow slab works like dielectric lens antenna (e.g., Lo & Lee, 1993). Let us make a rough estimate of the impact of this phenomenon on the increment Δz. For a spherical wavefront (dashed curve in Figure 2.5), the following equation is valid: *Ob=Oa+au+ug*. Dividing both sides of this equation by speed of the wave propagation, *c*, yields the time of the wavefront arrival at point *g*: $t_g^{(sp)} = \frac{Ob}{c} = \frac{Oa + au + ug}{c}$.

Due to delays in snow in part of *ag=au+ug* the equation for the wavefront arrival at point *g* is: $t_g^{(flt)} = \frac{Oa}{c} + \frac{au + ug}{v}$, where *v* is the wave speed in snow. Because *v*<*c*, $t_g^{(flt)} > t_g^{(sp)}$, providing proof of this flattening. To rate this phenomenon, let us suppose that the flattening front crosses the vertical at point *u*. This condition implies that the wave arrival times at points *u* and *b* are the same. This yields the equations: $\frac{Ob}{c} = \frac{Oa}{c} + \frac{au}{v}$ and $au = \frac{v}{c}(Ob - Oa) = \frac{v}{c} ag$. Hence, the relative shortage (flattening) of the wavefront path in the center of the beam compared with propagation in the free space (air) is equal to: $\frac{au}{ag} = \frac{v}{c} = \frac{1}{\sqrt{\varepsilon'}}$, and the corrected increment Δ*z* (2.11) should be decreased by $\sqrt{\varepsilon'}$ ~1.2…1.4 times.

Moreover, due to the increase in snow density with depth, the dielectric permittivity also increases, additionally impacting the rays' path configuration as takes place in a Luneburg lens. Thus, the actual meaning of the burial parameter lies between the two estimates carried out above:

$$d_b^{(flt)} \le d_b \le d_b^{(sp)} \tag{2.13}$$

Based on the above estimates, one can say that the surface sphericity practically contributes a relatively small amount to the estimate of the complete burial condition of the transverse dimension of the probing pulse, and consequently, the surface can be roughly considered as flat for any radar configurations regarding volume component assessment.

2.1.6. Modes of volume scattering for spherical wave

By analogy to spherical wave scattering from a surface (e.g., Moore & Williams, 1957) it is also reasonable to distinguish two modes of the volume component in the case of spherical wave scattering, as shown in Figure 2.6. For simplicity, the bounds of the snow slab are considered flat. Let us call the mode *depth-limited* (Figure 2.6a) if at the moment when the central point of the spherical wavefront reaches the bottom of a snow slab or a penetration depth (D_p), the peripheral point of the wavefront, crossing the surface, is still within the beamwidth footprint on the surface. This condition takes place when:

$$\frac{h}{R_0} \le \frac{1}{2}\left(\frac{\varphi_{0.5}}{2}\right)^2 \text{ if } h \le D_p \text{, or} \tag{2.14a}$$

$$\frac{D_p}{R_0} \le \frac{1}{2}\left(\frac{\varphi_{0.5}}{2}\right)^2 \text{ otherwise} \tag{2.14b}$$

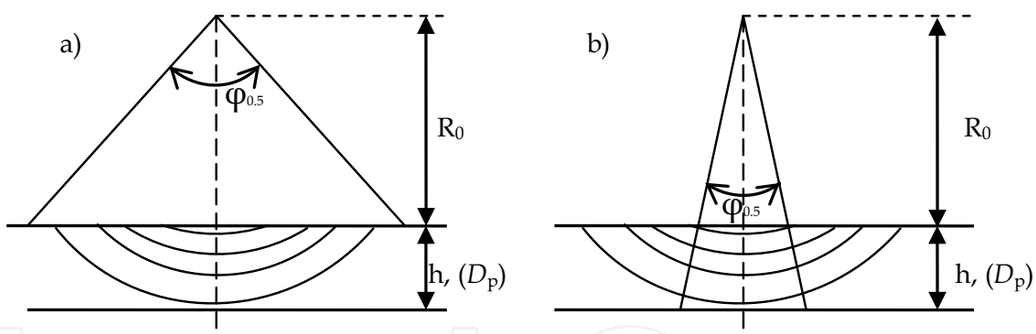

Fig. 2.6. Modes of the volume scattering; a) depth-limited, b) beamwidth-limited

Let us call the mode *beamwidth-limited* (Figure 2.6b) if the peripheral points of the spherical wavefronts, crossing the surface, are beyond the beamwidth footprint on the surface for a significant part of the scattering volume. This situation takes place when:

$$\varphi_{0.5} << 2\sqrt{2\frac{h}{R_0}} \text{ if } h \le D_p$$

or (2.15)

$$\varphi_{0.5} << 2\sqrt{2\frac{D_p}{R_0}} \text{ otherwise}$$

Obviously, that the depth-limited mode is inherent to space based altimeter and scatterometr and the beamwidth-limited mode is realized for SAR. If the "significant part" in the definition of this mode is replaced with a more exact term, the "determined part," the condition (2.15) can be modified and written in the form:

$$\varphi_{0.5} \le 2\sqrt{2\frac{h}{R_0}\left(1-\frac{\Delta h}{h}\right)} \text{ if } h \le D_p$$

or (2.15a)

$$\varphi_{0.5} \le 2\sqrt{2\frac{D_p}{R_0}\left(1-\frac{\Delta h}{D_p}\right)} \text{ otherwise}$$

where $\frac{\Delta h}{h}$ or $\frac{\Delta h}{D_p}$ is the relative part of the scattering volume in which the beamwidth-limited mode is fulfilled. For example, if 90% of the scattering volume ($\frac{\Delta h}{h}$ =0.9) is under the beamwidth-limited mode, the condition (2.15a) is $\varphi_{0.5} \le 2\sqrt{0.2\frac{h}{R_0}}$ for $h \le D_p$.

2.2. Condition of complete burial of radial size of the pulse volume

Suppose that some area of snow cover is illuminated by a radar located in orbit as shown in Figure 2.7. For simplicity, this scenario is depicted with a plane wavefront and flat surface.

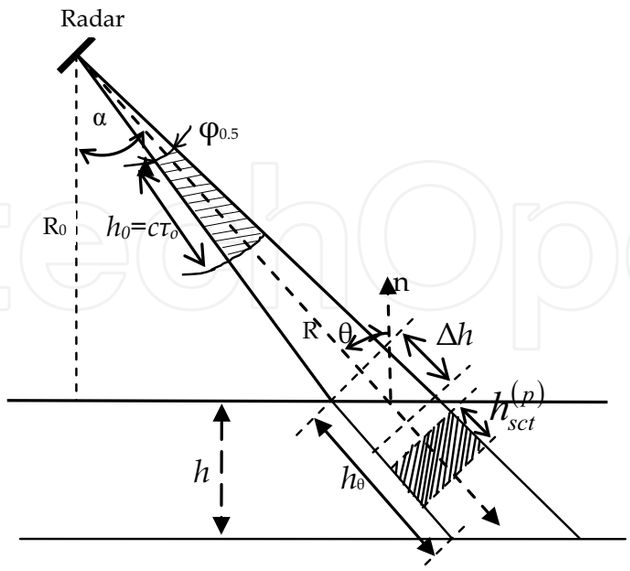

Fig. 2.7. Assessment of the complete burial of radial size of the probing pulse

Let us denote the height of the orbit as R_0, the distance from the radar to the center of the area as R, the anglular width of the main lobe of the antenna pattern as $\varphi_{0.5}$ and, the look angle as a. In addition, we assume that the cross-section of the main lobe is the circular. The illuminated area is assumed to be flat horizontally, and the bottom boundary surface of the snow slab is also flat and parallel to the top surface. Thus, the incidence angle, θ is equal to the look angle, α (θ=α).
The main scaling parameters determining radial propagation are:
1) The radial length of the pulse scattering volume, equal to half of its spatial extent in the snow medium:

$$h_{sct}^{(p)} = \frac{v\tau_0}{2} \tag{2.16}$$

where $v = \frac{c}{\sqrt{\varepsilon'}}$ is the wave propagation speed in snow, c is the wave propagation speed in the air, ε' is the real part of the snow permittivity and τ_0 is the duration of the probing pulse;
2) A one-way path in the snow, where the incidence power is decreased by "e" times, usually called the "penetration depth" in the literature

$$D_p = k_e^{-1} \tag{2.17}$$

where k_e is the extinction coefficient, which characterizes the attenuation properties of the medium due to scattering and absorption. One important remark is necessary. Since radar sounding of snow is often performed in off-nadir mode, and the main lobe of the antenna pattern has a finite angular size, it should be

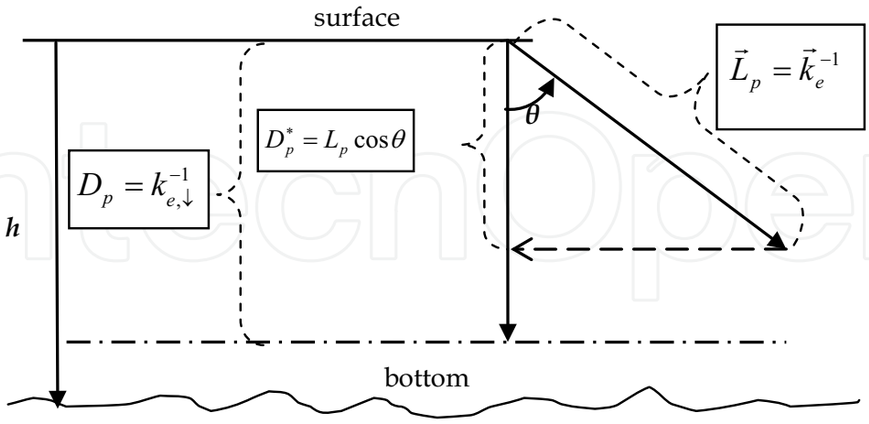

Fig. 2.8. Relationships between the penetration depth (D_p), penetration path (L_p) and propagation depth (D_p^*) in a snow slab

underlined that the extinction coefficient and the "penetration depth" are measured along the direction of the wave (ray) propagation and not only to the vertical. Therefore, calling the term $\propto k_e^{-1}$ as the "…depth" should be considered a little bit confusing. A more appropriate name for this term, from a physical point of view, is the "penetration path" (L_p), keeping in mind that the penetration depth (D_p) is its value in the vertical direction. The depth reached by an electromagnetic wave propagating at an angle θ to the vertical and attenuating by "e" times represents the vertical component of the penetration path, and can be called the propagation depth $\left(D_p^*\right)$, as illustrated in Figure 2.8. Thus, from this point onward in this paper, the following definitions and relationships are used:

$$\text{Penetration path: } \vec{L}_p = \vec{k}_e^{-1} \tag{2.18}$$

$$\text{Propagation depth: } D_p^* = L_p \cos\theta \tag{2.19}$$

$$\text{Penetration depth: } D_p = k_{e,\downarrow}^{-1} \tag{2.20}$$

where $k_{e,\downarrow}$ is the extinction coefficient in the vertical direction. In general, in inhomogeneous medium, the penetration path is a function of distance and direction $L_p = f\left(R,\theta,\psi\right)$, where ψ is the azimuthal angle. For homogenous medium $D_p = L_p$. We consider the probing pulse to be short if $h_{sct}^{(p)} \le L_p$; otherwise it is considered long. Obviously, the mode of sounding with current wave (CW) always belongs to the long probing pulse configuration. Also one should distinguish a case with fully scattering snow slabs, when the geometrical snow depth is equal to or less than the propagation depth ($h \le D_p^*$). Otherwise, one has a case of partially (because the wave does not penetrate to the bottom) scattering slow slab. The condition for complete burial, as it follows from Figure 2.7, is

$$h_{sct}^{(p)} \le h_\theta - \Delta h \tag{2.21}$$

where $h_\theta = \dfrac{h}{\cos\theta}$ is the slant snow depth and $\Delta h = 2R_0 tg\dfrac{\varphi_{0.5}}{2}\dfrac{tg\theta}{\cos\theta} \approx R_0\varphi_{0.5}\dfrac{tg\theta}{\cos\theta}$.

All of the above conditions are summarized in Table 2.1.

#	Condition	Description	Comments
1	$h_{sct}^{(p)} \le L_p$	Short/long probing pulse (P.P.)	Complete burial is satisfied for: a) short P.P. and fully scattering snow slab; b) long P.P. and partially scattering snow slab
2	$h \le D_p^*$ or $h_\theta \le L_p$	Fully/partially scattering snow slab	
3	$h_{sct}^{(p)} \le h_\theta - \Delta h$	Complete burial of the radial size of the probing pulse	

Table 2.1. Conditions for complete burial of the radial size of the probing pulse

Concluding remarks:
If the conditions for complete burial of the radial size of the probing pulse are completed, it can at least be said that one sample of the return signal is formed by the scattering volume

$$V_{sct} = h_{sct}^{(p)} A_{ill} \tag{2.22}$$

where A_{ill} is the illuminated base of the scattering volume. If, in addition, the conditions for complete burial of the transverse size of the probing pulse (see previous subsection) are also satisfied, that the scattering volume is determined by the entire pulse volume:

$$V_{sct} = V_p = h_{sct}^{(p)} \pi \left(R_0 \frac{\varphi_{0.5}}{2} \right)^2 \tag{2.23}$$

Otherwise, under $\Delta R \le \frac{1}{2} R_0 \left(\frac{\varphi_{0,5}}{2} \right)^2$,

$$V_{sct}(\Delta R) \approx h_{sct}^{(p)} 2\pi R_0 \Delta R \tag{2.24}$$

2.3. An assessment of the scattering volume under incomplete burial condition

If the parameters of the probing pulse and of the snow slab do not satisfy the conditions presented in the table above, the radial size of the scattering volume is determined by the geometry of the snow slab. Several practically important cases for practical application are discussed below.

2.3.1. Flat surface, plane wavefront, long probing pulse and fully scattering snow slab

In this scenario, the illuminated area, A_{ill} on the snow cover (Figure 2.1) is an ellipse, with the minor semi-axis equal to the radar beam cross-section radius $r_{\min} = \left(R \frac{\varphi_{0.5}}{2} \right)$ and major semi-axis the same divided by the cosine of the incidence angle: $r_{mjr} = {r_{\min}}/{\cos\theta}$. Thus:

$$A_{ill} = \pi \left(\frac{R\varphi_{0.5}}{2} \right)^2 \frac{1}{\cos\theta} \tag{2.25}$$

If one uses the height of the satellite orbit $R_0 = R\cos\theta$, (2.23) transforms to:

$$A_{ill} = \pi \left(\frac{R_0\varphi_{0.5}}{2} \right)^2 \frac{1}{\cos^3\theta} \tag{2.26}$$

The pattern of the scattering volume for this case is depicted in Figure 2.9, where the scattering volume is bounded by the surface and bottom planes.

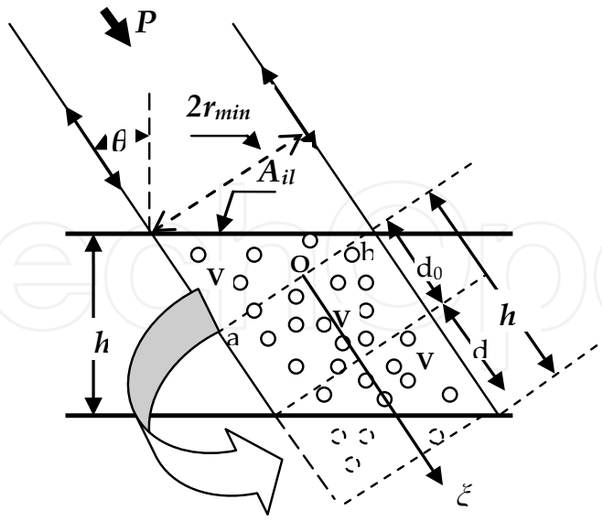

Fig. 2.9. An assessment of the scattering volume for a fully scattering snow slab

In this case, the size of the scattering volume is the sum of the volume of a circular cylinder V_0 with cylindrical element d_0 and two similar volumes of the truncated cylinders V_1 that mutually add up to a completed circular cylinder with cylindrical element d_1 (the bases of all volumes are the same and equal to $A_{ill}\cos\theta$):

$$V_{sct} = V_0 + 2V_1 = A_{ill}\cos\theta\left(d_0 + d_1\right) \tag{2.27}$$

Because $d_0 + d_1 = h_\theta$, we have, taking expression (2.25) into account:

$$V_{sct} = A_{ill}h = \pi h_\theta\left(\frac{R\varphi_{0.5}}{2}\right)^2 \tag{2.28}$$

Thus, the equivalent scattering volume is an elliptic cylinder with a base equal to the illuminated area on a surface and with a height element equal to the slab depth (under the assumption that the slab depth is less than the half of the spatial duration of the probe radar pulse). This result was obtained by Matzler (1987).

The duration of the SAR probing pulse duration is equal to several tens of microseconds (e.g., 42 μs for RadarSAT-1 and 37.1 μs for ERS-1). Due to frequency chirp, the compressed probing pulse duration decreases by many times, resulting in a volume radial size equal to only several meters (5-13 m for RadarSAT-1 and 9.7 m for ERS-1, for example). Numerical data are provided based on Alaska Satellite Facility documents ("RadarSAT-1 Standard Beam SAR Images", 1999; and "ERS-1 and ERS-2 SAR Images", 1996).

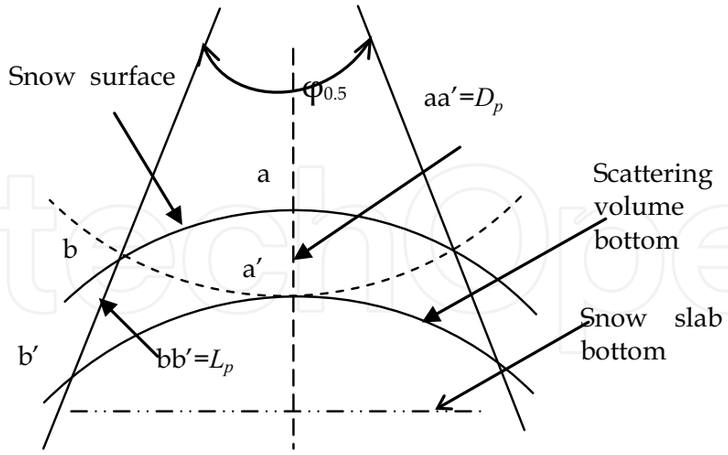

Fig.2.10. Cross-section of the scattering volume for a spherical surface and wavefront. The position of the flattened wavefront at the moment when its central point (a′) reaches the penetration depth is depicted with a convex dashed line

Because SAR images represent the backscatter pulse train from the entire path of a wave into a snow slab for any look angle as a point on a surface of some mean brightness (return power), the radial size of the scattering volume can be considered equal to either the slant size of the snow layer or the penetration path (whichever is smaller). That is, although the SAR pulse has a finite compressed spatial duration; it works like a long pulse due to the absence of radial discrimination in the sense of conventional radar terminology.

2.3.2. Long probing pulse, spherical wave, spherical surface, partially scattering slab

For this case, the bottom of the scattering volume is the geometrical placement of points located at a distance L_p from the snow surface along the family of rays within the solid angle of the main antenna lobe, as shown in Figure 2.10. The defining feature of this configuration is that the central and peripheral points of the spherical wavefront pass the length L_p at different times, resulting in different radii of curvature for the top and bottom bounded surfaces.

3. Volume component of the backscatter coefficient

3.1. Semi-empirical model for flat surface, plane wave and long probing pulse

Based on the considerations provided above, one can formulate an estimation of the volume component of the backscatter within the framework of the so-called semi-empirical model (Attema & Ulaby, 1978), as for the case of incomplete burial of the probing pulse with a flat surface, plane wave and a long probing pulse, which better fits the conditions for sounding of a thick snow slab with SAR.

The total radar backscatter from the illuminated area is composed of four components (Fung, 1994):

$$\sigma_t = \sigma_{as} + \sigma_s + \sigma_g + \sigma_{gv} \tag{3.1}$$

where σ_{as} is the radar cross-section (RCS) due to backscatter from the air/snow (top) interface, σ_s is the RCS due to backscatter from the snow volume, σ_g is the RCS due to backscatter from the snow/ground (bottom) interface and σ_{gv} is the RCS due to rescattering between ground and snow volume irregularities. As was summarized by Koskinen (2001), only the volume component is essential for dry snow. Therefore the essential portion of the total backscatter consists of the volume component and the contribution of the ground beneath:

$$\sigma_t = \sigma_s + \sigma_g \tag{3.2}$$

Obviously, the radar becomes sensitive to the properties of the snow only when $\sigma_s >> \sigma_g$. In accordance with Ulaby et al. (1982), the general form for the backscatter coefficient from a surface is:

$$\sigma_t^0 = \frac{\sigma_t}{A_{ill}} \tag{3.3}$$

This notation presupposes that the illuminated areas on the slab top and on the ground (bottom of the slab) are the same. This assumption applies for small angle divergences of the radar beam, as is valid for strong directed antennae, low refraction on the air-snow interface and a ground surface that is flat and parallel to the surface of the snow slab. Accordingly, the volume component of the backscatter coefficient is:

$$\sigma_s^0 = \frac{\sigma_s}{A_{ill}} \tag{3.4}$$

In the incoherent approach, $\sigma_s = \sum_{i=1}^{N} \sigma_i$; i.e., σ_s represents the total radar cross-section (RCS) of N scatterers contributing backscatter from a volume $V_{sct} = A_{ill} h$ of a snow slab (see subsection 2.3.1). Due to attenuation of the electromagnetic wave upon propagation within a snow mass, the total RCS of the snow slab is equal to:

$$\sigma_s = \sum_{i=1}^{N} \sigma_i \alpha_i \tag{3.5}$$

where the attenuation coefficient, inherent to the *i-th* particle with a distance of ξ_i from the coordinate origin O, is equal to:

$$\alpha_i = \exp\left(-2 k_e \xi_i\right) \tag{3.6}$$

where k_e is the extinction coefficient. The factor α takes into account the two-way distance of forth and back wave propagation. The assessment of the scattering volume described above relates only to the absolute value of the volume. In the case of wave directed propagation and, consequently, directed attenuation, the summation should be performed along the

propagation axis, ξ. Because N>>1, the summation in (3.5) can be replaced by integration. As was mentioned above, this integration should be carried out along the direction of wave propagation, i.e., along the ξ axes. Small changes in the propagation direction at the air/snow interface are ignored due to minor differences in the corresponding refraction coefficients. Due to the random spatial distribution of scatterers within the scattering volume, this discussion considers only the mean backscatter characteristics averaged over several illuminated areas, with particles having independent spatial locations and RCSs.

$$\left\langle \sigma_s \right\rangle = \left\langle \sum_{i=1}^{N} \sigma_i \alpha_i \right\rangle = \left\langle \int_0^{h_\theta} \sigma(\xi)\,\alpha(\xi) d\xi \right\rangle = \int_0^{h_\theta} \left\langle \sigma(\xi) \right\rangle \alpha(\xi) d\xi \tag{3.7}$$

where $\sigma(\xi)$ is the running RCS (by the unit of a distance along axis ξ, dimension is $\left[\frac{L^2}{L}\right]$) of the scattering volume. Assuming that the attenuation properties of snow remain the same along the propagation path $(k_e \neq f(\xi))$, one can write:

$$\alpha(\xi) = \exp(-2k_e\xi) \tag{3.8}$$

If the scatterers' RCSs are independent of their locations within the scattering volume (condition of incoherent approach), we get:

$$\left\langle \sigma_s \right\rangle = \left\langle \sigma \right\rangle \int_0^{h_\theta} \alpha(\xi) d\xi \tag{3.9}$$

where <σ> is the mean running RCS of the scattering volume.
Based on (3.4) and taking into account (3.9), the mean backscatter coefficient can be written as:

$$\left\langle \sigma_s^0 \right\rangle = \frac{\left\langle \sigma_s \right\rangle}{A_{ill}} = \frac{\left\langle \sigma \right\rangle}{A_{ill}} \int_0^{h_\theta} \alpha(\xi) d\xi \tag{3.10}$$

Taking into account that h_θ is the radial size of the scattering volume (along axis ξ), $\left\langle \sigma_s^* \right\rangle = \left\langle \sigma \right\rangle \cdot h_\theta$ is the mean total RCS of snow (ice) particles within the scattering volume (an oblique cylinder) while ignoring the attenuation and $\left\langle \sigma_v \right\rangle = \frac{\left\langle \sigma_s^* \right\rangle}{V}$ is the corresponding mean volume specific backscatter coefficient, we can transform the ratio $\left\langle \sigma \right\rangle / A_{ill}$ to the form:

$$\frac{\left\langle \sigma \right\rangle}{A_{ill}} = \frac{\left\langle \sigma \right\rangle}{A_{ill}} \cdot \frac{h_\theta}{h_\theta} = \frac{\left\langle \sigma \right\rangle h_\theta}{A_{ill} h} \cos\theta = \frac{\left\langle \sigma_s^* \right\rangle}{V} \cos\theta = \left\langle \sigma_v \right\rangle \cos\theta \tag{3.11}$$

Therefore, substituting (3.11) into (3.10), we can state:

$$\left\langle \sigma_s^0 \right\rangle = \left\langle \sigma_v \right\rangle \cos\theta \int_0^{h_\theta} \alpha(\xi) d\xi \tag{3.12}$$

Taking into account (3.8) and assuming the homogeneity of snow slab $\left(k_e \neq f\left(\xi,\theta,\psi\right)\right)$, we can conduct the integration of (3.12) and finally arrive at:

$$\left\langle \sigma_s^0 \right\rangle = \left\langle \sigma_v \right\rangle \frac{1}{2k_e}\left[1-\exp\left(-2k_e h_\theta\right)\right]\cdot\cos\theta \tag{3.13}$$

This expression is the mathematical formulation of the semi-empirical model and has been obtained by Attema & Ulaby (1978) and Ulaby et al. (1982). In this paper, this model will be cited as the "A-U model." For this case, the backscatter coefficient (3.13) depends only on the specific volume backscatter of the snow medium and not on the pulse volume sizes. This remarkable feature is due to (1) "overcomplete" burial of the pulse length into the snow medium, and (2) the backscattering normalization factor A_{ill} (see 3.4) is the basis of the probing pulse.

The obvious imperfection of the model, as applied to sounding of thick snow, is the assumption of a constant extinction coefficient within the snow slab. The problem can be solved by designing an appropriate stratification model for the selected study area and modeling the spatial distribution of the extinction coefficient (e.g., Drinkwater et al., 2001).

The next limitation of the model is due to wave sphericity. Under depth-limited mode conditions (see section 2), the illuminated area changes, and the running RCS in (3.7) can not be assumed to be statistically homogeneous within the scattering volume. The same is true regarding the extinction coefficient in (3.8) as well. Thus, for this case, the A-U model in form (3.13) should be used with care. For the beamwidth-limited mode, the form in (3.13) can be used, taking in mind the "determined part" of the scattering volume (see comments to 2.15a).

The ground component of the backscatter coefficient is localized by the bottom location and can thus be expressed by its backscatter coefficient, taking into account the attenuation:

$$\sigma_g^0 = \sigma_{g,\max}^0 \exp\left(-2k_e h_\theta\right) \tag{3.14}$$

where $\sigma_{g,\max}^0$ is the backscatter coefficient of the ground bottom surface governed only by the surface properties and its orientation in regards to the incidence of radar illumination..

3.2. Effective snow depth

Given the expression

$$\frac{1}{2}L_p\cos\theta\left[1-\exp\left(-2\frac{h}{L_p\cos\theta}\right)\right] = H_{eff} \tag{3.15}$$

(3.13) can be presented in the simple form:

$$\left\langle \sigma_s^0 \right\rangle = \left\langle \sigma_v \right\rangle H_{eff} \tag{3.16}$$

where H_{eff} is the effective depth of snow sounding (EDS); i.e., the depth such that the backscatter from which occurs as if without attenuation, with backscatter equal to that which would occur from a slab of larger real depth with attenuation due to absorption and scattering.

Parameter $k_e h_\theta = \frac{h_\theta}{L_p} = \tau_\theta$ is the optical thickness of snow (SOT) along the wave propagation direction. It is useful to express the backscatter coefficient through the dimensionless EDS using the geometrical snow depth, h: $H_{eff}^0 = {H_{eff}}/{h}$. Given that expression, equation (3.16) can be written in the form:

$$\left\langle \sigma_s^0 \right\rangle = \left\langle \sigma_v \right\rangle h H_{eff}^0 = \left\langle \sigma_s^0 \right\rangle_{\max} H_{eff}^0 \tag{3.17}$$

where

$$\left\langle \sigma_s^0 \right\rangle_{\max} = \left\langle \sigma_v \right\rangle \cdot h \tag{3.18}$$

is the maximal value of the backscatter coefficient for a given snow depth, h, ignoring both energy losses due to attenuation and scattering and the angular dependence of the scattering volume. The normalized effective depth of snow sounding (nEDS≡ H_{eff}^0) plays the role of a correction factor, and is equal to:

$$H_{eff}^0 = \frac{1}{2\tau_\theta}\left[1 - \exp\left(-2\tau_\theta\right)\right] \tag{3.19}$$

And the main formula of the model (3.2) can be written as:

$$\sigma_s^0 = \left\langle \sigma_s^0 \right\rangle_{\max} \cdot H_{eff}^0 + \sigma_g^0 \tag{3.20}$$

It is useful to find the dependence of the correction factor on the SOT magnitude and the incidence angle. Let us consider two extreme cases:

a) "shallow" snow: $\tau_\theta << 1$

$$H_{eff}^0 \approx \frac{1}{2\tau_\theta}\left[1 - \left(1 - 2\tau_\theta\right)\right] = 1 \tag{3.21}$$

Given this relation,

$$\left\langle \sigma_t^0 \right\rangle = \left\langle \sigma_v \right\rangle h + \sigma_g^0 \tag{3.22}$$

meaning that the EDS is approximately equal to the geometrical snow depth. Nevertheless,

the small magnitude of the volume component compared with the backscatter from the bottom layer ($\langle\sigma_v\rangle h < \sigma_g^0$) makes this dependence difficult to use in practice. For example, a snow layer with h<~1 m is practically transparent to electromagnetic irradiance of the C-band.

b) "thick" snow: $\tau_\theta >> 1$

$$H_{eff}^0 \approx \frac{1}{2\tau_\theta} = \frac{L_p \cos\theta}{2h} = \frac{1}{2}\frac{D_p^*}{h} \tag{3.23}$$

Given this relation, and in accordance with (3.18) and (3.20), one gets:

$$\left\langle \sigma_t^0 \right\rangle = \left\langle \sigma_s^0 \right\rangle_{\max}^* + \sigma_g^0 \tag{3.24}$$

where $\left\langle \sigma_s^0 \right\rangle_{\max}^* = \frac{1}{2}\langle\sigma_v\rangle D_p^*(\theta)$. Equation (3.24) shows that the backscatter depends only on the penetration path (depth) under a constant incidence angle. In the "thick" snow regime, no additional snow accumulation contributes to the total backscatter due to the saturation effect. On the other hand, in this regime, the backscatter coefficient demonstrates an angular dependence, as the angle of incidence affects the propagation depth (D_p^*). The sensitivity of the backscatter coefficient to the changes in snow thickness takes place in the so-called "intermediate" regime, when $\tau_\theta \sim 1$. Field data gives 20-30 meters of the penetration depth for the C-band (e.g., Hoen & Zebker, 2000), and yield values that can be considered the "working" range for probable snow measurements in this wave band. Values of the nEDS (3.19) can be assessed from the plot of the nEDS as a function of SOT, as shown in Figure 3.1.

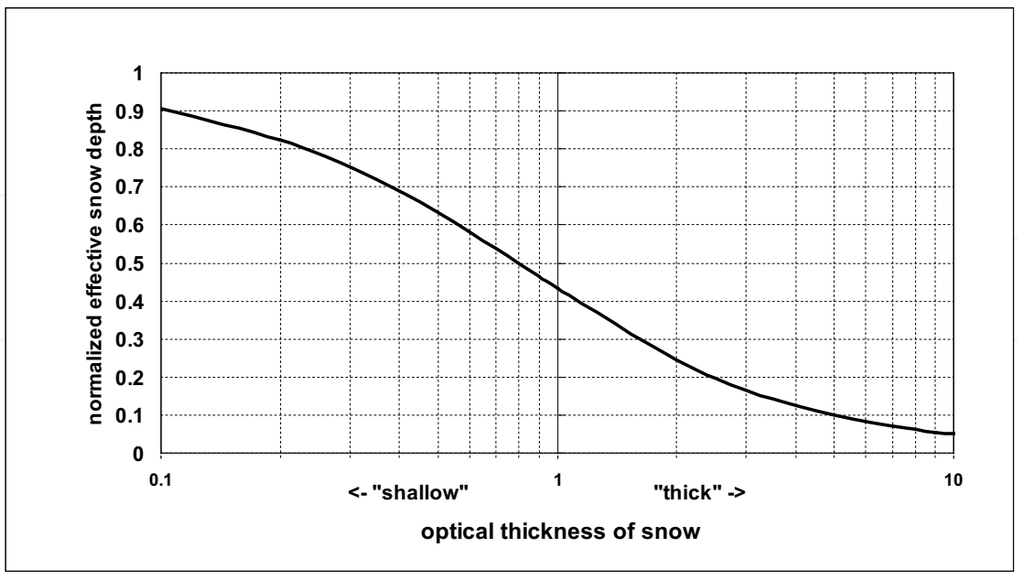

Fig. 3.1. Plot of the normalized effective depth of snow sounding versus the snow optical thickness

To evaluate the angular dependence of the nEDS, we consider the normalized Snow Depth (nSD), which is the depth of snow normalized to the penetration path:

$$nSD = \frac{h}{L_p} \tag{3.25}$$

Comparing nSD with the definition of the SOT yields:

$$nSD = \tau_\theta \cdot \cos\theta \tag{3.26}$$

Substituting (3.26) into (3.19), we have

$$H^0_{eff} = \frac{1}{2}\frac{\cos\theta}{nSD}\left[1 - \exp\left(-2\frac{nSD}{\cos\theta}\right)\right] \tag{3.27}$$

A plot of (3.27) reduced to zero dB at θ=0 for different nSD is shown in Figure 3.2. As follows from this plot , the angular dependence of the volume component of the backscatter coefficient in a practically appropriate range of angles, 0-50^0 is rather weak and equal to ~2dB for the thick snow regime. For the intermediate regime, with nSD~1, its range of variation is about 1 dB. Because this range is of the same order as the errors, it is difficult to expect a notable angular dependence in practical measurements inherent to the intermediate regime.

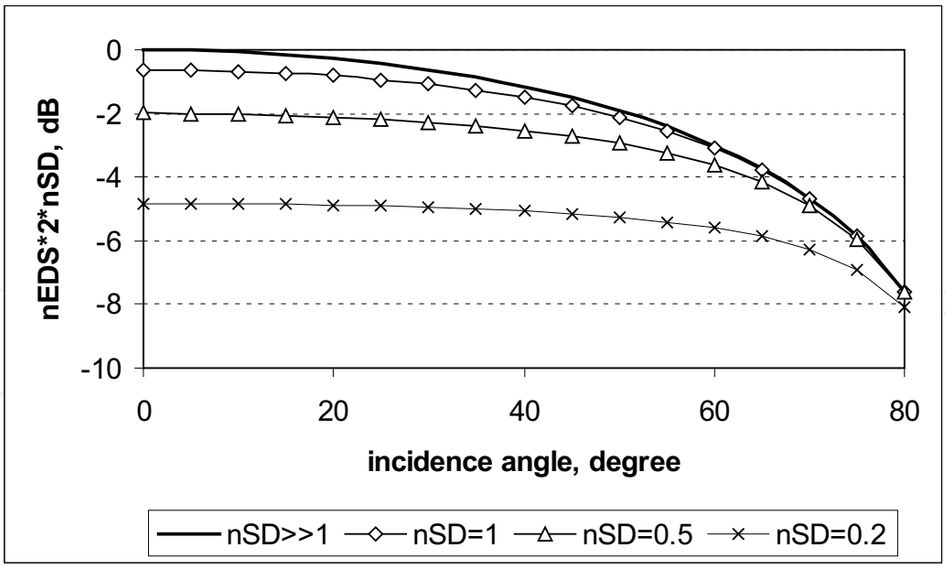

Fig. 3.2. The angular dependence of the normalized effective depth of snow sounding for the "thick" (nSD>>1) and "intermediate" regimes

On the other hand, a notable angular dependence of the backscatter coefficient indicates that snow depth is greater than the penetration path. The intermediate regime represents practical interest for snow measurements. Suppose, for instance, the linear dependence of the geometrical snow depth on a horizontal distance *S* over the flat surface:

$$h(s) = k \cdot S \tag{3.28}$$

where *k* is the proportionality factor. Given that relation and taking into account (3.18) - (3.20), the normalized backscatter coefficient as a function of a distance is:

$$\frac{\sigma_s^0(S)}{\langle \sigma_s^0 \rangle_{\max}} = \frac{1}{2}\cos\theta\left[1 - \exp\left(-2\frac{k \cdot S}{D_p^*(S,\theta)}\right)\right] \tag{3.29}$$

To specify the proportionality factor, let us assume that the geometrical snow depth reaches the propagation depth value at a distance, for example, equal to S_0, i.e., $k = \frac{D_p^*}{S_0}$. Thus,

$$\frac{\sigma_s^0(S)}{\langle \sigma_s^0 \rangle_{\max}} = \frac{1}{2}\cos\theta\left[1 - \exp(-2S')\right] \tag{3.30}$$

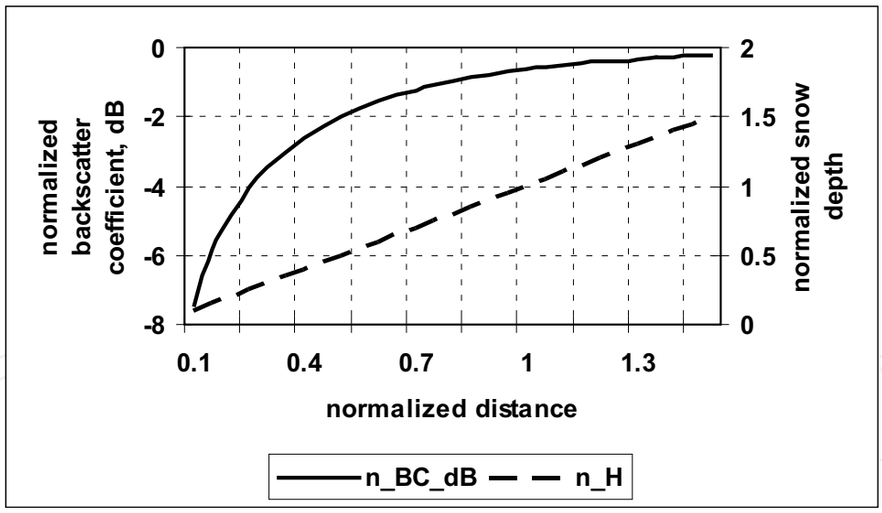

Fig. 3.3. Illustration of the expected relative spatial behavior of the backscatter coefficient under a linear dependence of the snow depth on a distance

where $S' = \frac{S}{S_0}$ is the normalized distance. For the intermediate regime, we can ignore the angular dependence of the backscatter coefficient. Let us also assume that the specific volume scattering is approximately the same for all points along that distance. The

corresponding plot of expression (3.27), additionally normalized by a factor of $\frac{2}{\cos\theta}$, is depicted in Figure 3.3:

$$\frac{2}{\cos\theta}\frac{\sigma_s^0(S)}{\left\langle\sigma_s^0\right\rangle_{\max}} = 1-\exp(-2S') \tag{3.31}$$

Thus, in accordance with the semi-empirical model, the expected profile of the backscatter coefficient should have an exponential pattern for a transect taken over terrain with a linear increase in snow depth within the intermediate regime condition.

4. Comparison the A-U model estimates and the experimental radar data on the Greenland ice sheet

For accurate comparison of the model with any experimental data, the study area must satisfy the "thick" snow condition to exclude the impact of the ground. Second, the snow pack must contain primarily Rayleigh ice particles with sizes less than approximately one-tenth of the wavelength. The most appropriate area matching this condition is the dry snow zone of the Greenland ice sheet. This region is not impacted by melt-freezing processes due to permanent sub-zero temperatures year-round. Therefore, the auspicious conditions for creation the ice lenses, tubes and large size aggregates, which inherent, for instance, to the percolation zone, are absent here. Additionally, the snow (firn) is up to several tens of meters deep (e.g., Zwally & Brenner, 2001), corresponding to the intermediate or even the thick snow regime. Due to known difficulties regarding *in situ* measurements in Greenland, there are no examples of the comparison of backscatter with snow depth in the literature for the intermediate or thick snow regimes.

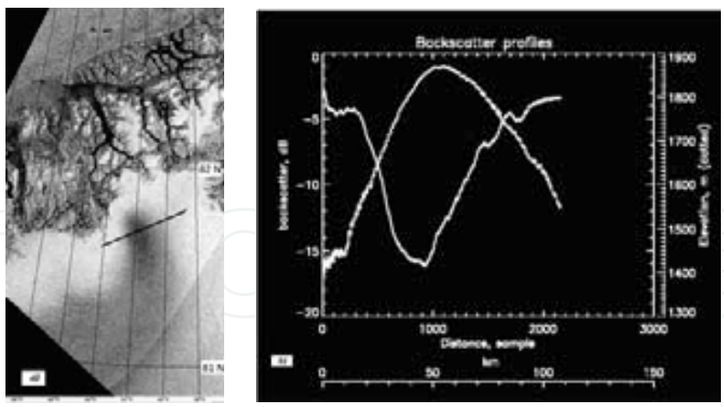

Fig. 4.1. Transect across hill (straight line crossing the dark spot on the SAR signature) in the north-eastern region of Greenland (left), and the corresponding backscatter (solid line, convex downwards curve) and elevation (dotted line, convex upwards curve) profiles (right)

Nevertheless, a certain qualitative example of the sensitivity of backscatter to the snow depth relative to the intermediate regime can be provided based on a topographic feature (a hill) in the northeast region of Greenland between 81^0 and 82^0 N, as shown in Figure 4.1.

The counter-phase behavior of the backscatter coefficient and the elevation profiles plotted above can be explained supposing that the snow depth is minimal on the hilltop and increases proportional to the distance from the top of the hill down to its base. This assumption closely matches the field and modeled data provided by Jaedicke et al. (2000).
For quantitative assessment of the semi-empirical model more regular terrain should be chosen. A typical dry snow area is presented on the RadarSAT-1 SAR image of eastern Greenland in Figure 4.2.
As is clearly seen, the magnitude of the backscatter coefficient is about -20 dB in the dry snow zone. This assessment coincides with data in the known literature (e.g., Drinkwater et al., 2001; Partington, 1998; Baumgartner et al., 1999; Forster et al., 1999) which also gives values of -12…-20 dB. We can estimate the corresponding value using the A-U model. We assume that the thick snow regime is valid, and that the snow slab consists primary of particles of roughly the same sizes; i.e., it is a monodisperse medium.
For these conditions (see 3.24), ignoring backscatter from the bottom surface, we get:

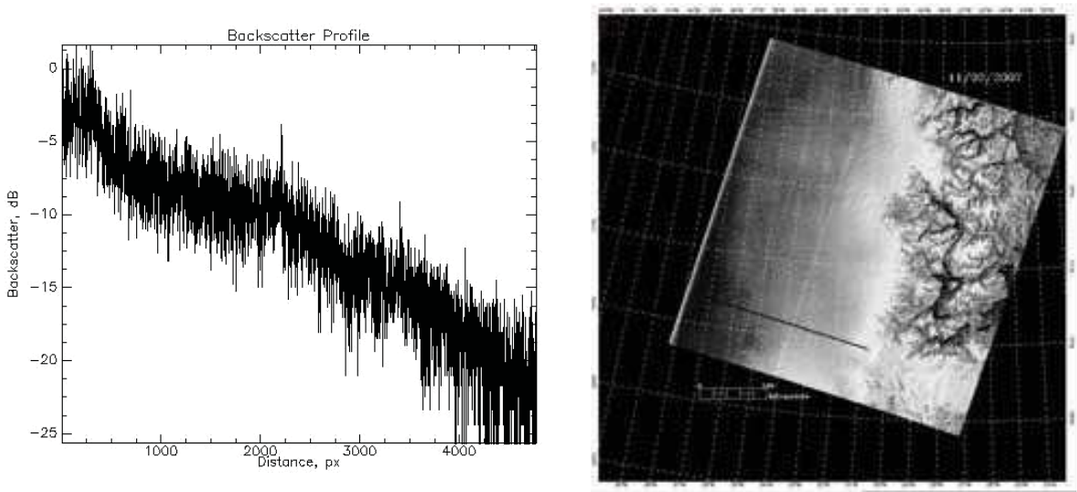

Fig.4.2. Illustration of the backscatter coefficient values (left) range for an arbitrary transect (straight line on RadarSAT-1 SAR signature, right) from the percolation to the dry snow areas within the east margin of the Greenland Ice Sheet (directions are from left to right for the plot of the backscatter profile and contra versa for the SAR signature; date of data acquisition: November 2, 2007; data granule ID: R1_62609_SWB_271)

$$\sigma_s^0 = \sigma_v \frac{L_p \cos\theta}{2} = \frac{1}{2}\sigma_v \frac{\cos\theta}{k_e} \tag{4.1}$$

Further calculations below aim to discover the specific volume backscatter, σ_v and the extinction coefficient, k_e. The estimates listed below will be conducted with the Rayleigh approach. In accordance with Ulaby et al. (1986), this approach bounds the upper electric size of particle, $\zeta_u = \frac{2\pi r_u}{\lambda}$, with the inequality $\zeta_u |\dot{m}| \le 0.5$, where m is the complex refractive index of the particle matter and r_u is the corresponding upper size of a particle. For ice particles with $|\dot{m}| \approx 1.7776$ observed with C-band radar (λ=5.6 cm), the maximal size

satisfying the Rayleigh approach is 2.6 mm. Following known relationships (e.g., Ulaby et al, 1986), the specific volume scattering is:

$$\sigma_v = Z_s \frac{1}{\lambda^4} \tag{4.2}$$

where

$$Z_s = \frac{2^6}{V}\pi^5 \left|K\right|^2 \sum_{i=1}^{N} r_i^6 \tag{4.3}$$

In this formulae

$$\left|K\right|^2 = \left|\frac{\dot{m}^2 - 1}{\dot{m}^2 + 2}\right|^2 \tag{4.4}$$

where $\dot{m} = n + j\eta$ is the refractive index of the particle matter and n and η are the real and imaginary parts of the refractive index, respectively. The value of these components can be derived from the value of the complex dielectric permittivity of a material $\dot{\varepsilon} = \varepsilon' + j\varepsilon''$, where ε′ and ε'' are the real and imaginary parts of the dielectric permittivity.

$$n = \left[0.5 \cdot \left(\sqrt{(\varepsilon')^2 + (\varepsilon'')^2} + \varepsilon'\right)\right]^{0.5} \tag{4.5}$$

$$\eta = \left[0.5 \cdot \left(\sqrt{(\varepsilon')^2 + (\varepsilon'')^2} - \varepsilon'\right)\right]^{0.5} \tag{4.6}$$

For monodisperse media (r_i=r) equation (3.3) has the form:

$$Z_s = 2^6 \pi^5 \left|K\right|^2 n^0 r^6 \tag{4.7}$$

where n^0 is the particle concentration.
The extinction coefficient can be calculated as a sum of the absorption (k_a) and scattering (k_s) coefficients (Ulaby et al., 1986):

$$k_e = k_a + k_s = n^0 \left[Q_a + Q_s\right] \tag{4.8}$$

where Q_a and Q_s are the absorption and scattering cross-sections respectively. These parameters, under the Rayleigh approach, can be calculated by the following formulas:

$$Q_a = \frac{\lambda^2}{\pi}\zeta^3 \operatorname{Im}\{-K\} \tag{4.9}$$

and

$$Q_s = 2\frac{\lambda^2}{3\pi}\zeta^6 \left|K\right|^2 \tag{4.10}$$

In accordance with (Ulaby et al., 1982)

$$\mathrm{Im}\{-K\} \approx \frac{3\varepsilon''}{(\varepsilon'+2)^2} \tag{4.11}$$

The real part of the dielectric permittivity for ice, contained in the formulas above, is equal to 3.15 and in practice does not depend on temperature or wavelength. The imaginary part of the dielectric permittivity for ice is not constant with changes in temperature or the illumination frequency. In accordance with Matzler (1987) it can be expressed through the following empirical formula:

$$\varepsilon'' = \frac{A}{F} + BF^C \tag{4.12}$$

where F is frequency in GHz and A, B and C are the empirical coefficients. For a temperature of -15^{0}C, which is more appropriate for the dry snow case, the coefficients are equal to: A=3.5*10^{-4}, B=3.6*10^{-5}, C=1.2. Now, the expressions obtained for the backscatter coefficient calculation may be combined. Substituting (4.2) in (4.1), we get:

$$\sigma_s^0 = \left(\frac{1}{2}\frac{Z_s}{\lambda^4 k_e}\right)\cos\theta \tag{4.13}$$

Taking into account (4.7) and (4.8)-(4.10), one can get:

$$\sigma_s^0 = \frac{1}{2\lambda^4}\frac{2^6\pi^5|K|^2 n^0 r^6}{n^0\left[\frac{\lambda^2}{\pi}\zeta^3\,\mathrm{Im}\{-K\} + \frac{2\lambda^2}{3\pi}\zeta^6|K|^2\right]}\cos\theta \tag{4.14}$$

Simplifying this expression, we have:

$$\sigma_s^0 = \frac{1}{2}\frac{\cos\theta}{\frac{1}{\zeta^3|K|^2}\mathrm{Im}\{-K\} + \frac{2}{3}} \tag{4.15}$$

An important feature of this expression is its independence with regards to the particle concentration, a reflection of the property inherent to the saturation regime mentioned above in section III. Since the scattering volume is less than the spatial duration of the probing pulse an increasing particle number is equivalent to an increasing particle concentration. Thus, no additional amount of the snow over the snow pack with a thickness greater than the penetration depth can cause a notable increase in the backscatter coefficient. This circumstance is also very useful from a simulation point of view, since there is no microstructure parameter that needs to be assumed. For the numerical calculation listed below we assumed that the snow within the dry snow zone consists of snow grains that are actually grains of ice that look like grains of rice, with a typical size of ~1 mm. Taking into account the fact for ice: ε′=3.15 and ε′>> ε″ (Tiuri et al., 1984; Matzler, 1987), $|K|^2 = 0.16$.

Given that information, equation (4.15) for an intermediate incidence angle of ~40^0 (cosθ=0.77) is equal to:

$$\sigma_s^0 = \frac{0.385}{\frac{6.25}{\zeta^3}\mathrm{Im}\{-K\}+\frac{2}{3}} \tag{4.16}$$

Taking into account (4.11) and (4.12), we get:

$$\sigma_s^0 = \frac{0.5775}{\frac{1.06}{\zeta^3}\left(\frac{A}{F}+BF^C\right)+1} \tag{4.17}$$

The plot of (4.17) is depicted in Figure 4.3 for C-band radar with F=5.3 GHz ($\lambda\approx$ 5.6 cm).

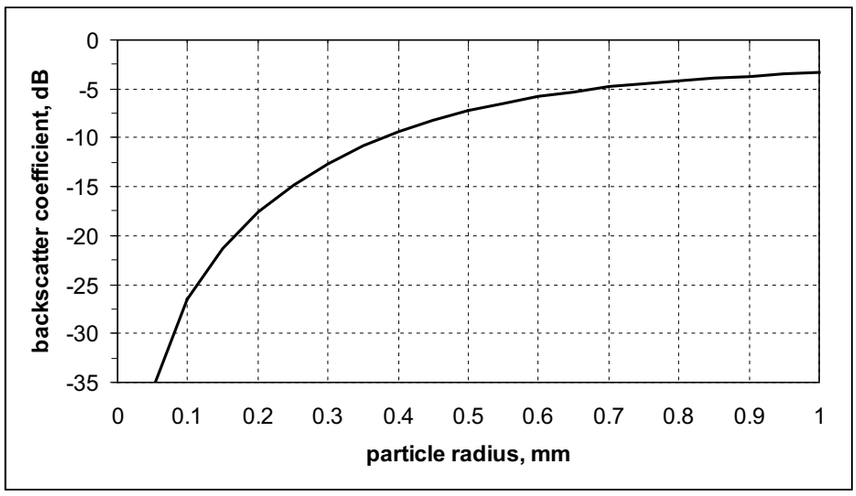

Fig. 4.3. The dependence of the backscatter coefficient on particle size in accordance with the A-U model for C-band radar and snow depth greater than the penetration depth ("thick" snow regime)

It follows from this plot that the observable backscatter coefficient values of -12…-20 dB can be caused by particles with radii of less than 0.35-0.17 mm. The current estimates are slightly lower compared with the same made by Partington (1998), who found that the backscatter coefficient would range from -20 dB for a mono-distribution of grain sizes with a mean radius of 0.25 mm to -2 dB for a mean grain radius of 1 mm. Our results showed a 0.17 mm mean radius for -20 dB and a 1 mm mean radius for -3 dB. The small discrepancy is probably due to the temperature dependence of the imaginary part of the ice's dielectric permittivity. The grain sizes values assessed do not coincide with the field data. In accordance with Table 4.1, the mean particle radius within a ~1 m depth surface layer of dry snow is 0.5…2.0 mm. As seen in Figure 4.3., these values should produce a backscatter coefficient of approximately from -8 dB to 0 dB. Thus, there is a discrepancy of ~12 dB between the observable data and the values forecast by the semi-empirical model. Therefore,

the A-U model overestimates the backscatter coefficient significantly. It should be noted, in addition, that the particle radius can only increases with the snow depth due to the depth-dependent grain radius model (Alley et al., 1982):

$$r^2(h) = r_0^2 + \frac{C \cdot h}{H_a} \tag{4.18}$$

where r_0 is the mean radius at the surface, C is the crystal growth rate and H_a is the mean annual layer thickness. Given this model, various simulation experiments (e.g., Forster et al., 1999; Drinkwater et al., 2001) and field measurements (e.g., Jezek et al., 1994; Woods, 1994; Lytle & Jezek, 1994), the mean particle radius for the entire scattering volume is even greater than the surface values and the aforementioned discrepancy becomes even more firmly grounded.

#	Mean ice particle radius, mm	Source	Location
1	0.5-2.0	Benson, 1996	Greenland
2	1.0-1.5	Schytt, 1964	Spitsbergen
3	Less than 0.75 mm	Higham and Craven, 1997	Antarctic
4	0.2-0.6	Woods, 1994	Greenland
5	0.1-0.7	Lytle and Jezek, 1994	Greenland

Table 4.1. Literature data on the mean ice particle size near the surface of dry snow cover

Thus, although the A-U model gives a qualitative assessment of the main features of backscatter behavior from a snow slab, the result of quantitative comparisons with field data does not match the theoretical predictions.

5. Enhanced semi-empirical model of the volume component of the backscatter coefficient

The problem highlighted in the previous section can be resolved by considering the statistical properties of the small-scale fluctuations in the particle concentration and its scattering properties within the scattering volume. The appropriate method for doing so that is the so-called "slice" approach, which was primarily suggested in weather radar meteorology (Marshal & Hitchfeld, 1953; Smith, 1964). This approach exploits the known radar feature in accordance with which the particles of a "cloud" located close to the front of the incident radar wave are considered to be approximately at the same distance from the radar and reflect incident electromagnetic wave almost coherently. One can consider that these particles are embedded in a fictitious thin cylindrical volume ("slice"), whose base coincides with the surface of spherical wave front and side-bounded by the main lobe of the antenna pattern. Thus, the scattering volume into a snow slab can be represented as an adjoining series of these slices, as illustrated in Figure 5.1. Each slice is much narrower than the radar wavelength in the wave propagation direction ($\Delta_s << \lambda$).

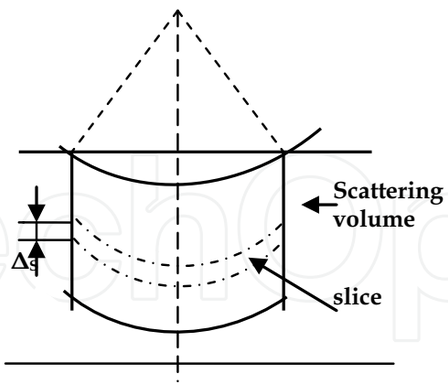

Fig.5.1. Simplified slice approach scheme. The arbitrary position of a single slice is shown on the cross section of the scattering volume

A slice's radial size, Δ_s can actually be considered as a minimal spatial scale of the backscatter property fluctuation, if this scale is much smaller than the wavelength. Using this approach, it was shown by the author (Yurchak, 2009), that the specific volume component of the backscatter from any spatial extended geophysical target (SEGT), included the snow as well, can be presented as the incoherent sum of the radar cross-sections of individual scatterers only if the number of particles in the slices (n) are distributed in accordance with the Poisson law; i.e., the variance of the number of particles ($Var(n)$) is equal to the mean number ($\langle n \rangle$). Otherwise, the "classical" specific volume component should be corrected by a so-called deviation factor $Y(\xi_a, \chi)$:

$$\langle \sigma_v \rangle = \langle \sigma_v \rangle_{class} Y(\xi_a, \chi) \tag{5.1}$$

where

$$Y(\xi_a, \chi) = \frac{\xi_a^2 + \chi}{\xi_a^2 + 1} \tag{5.2}$$

and $\chi = \frac{Var(n)}{\langle n \rangle}$ is the Poisson index, $\xi_a = \frac{Stdev(a)}{\langle a \rangle}$ is the variation coefficient of the particle radar equivalent length (PREL $a_p \equiv \sqrt{\sigma_p}$, σ_p is the radar cross-section of an individual particle). Formulas (5.1) and (5.2) reflect the fundamental physical principal that the fluctuations of the medium parameters (inhomogeneities) are the cause of the electromagnetic wave scattering (e.g., Atlas, 1964; Fabelinskii, 1968). The parameter ξ_a might be expressed through the measurable parameters of the snow particle size distribution function (PSDF), such as the variation coefficient of particle radius, $\xi_r = \frac{Stdev(r)}{\langle r \rangle}$, and the skewness coefficient, Sk:

$$\xi_a = 3\xi_r^{-3/2} \frac{\sqrt{\xi_r^{-1} + 2 \cdot Sk}}{\xi_r^{-3} + 3\xi_r^{-1} + Sk} \tag{5.3}$$

Following Shi et al. (1993), if the PSDF for snow can be presented by the lognormal distribution, the parameters of relationship (5.3) are: $\xi_r = \sqrt{\exp(S_r^2) - 1}$, and $Sk = \sqrt{\exp(S_r^2) - 1} \cdot [2 + \exp(S_r^2)]$. Given these relations, $Sk = \xi_r^3 + 3\xi_r$. Thus, the PREL variation coefficient (5.3) depends, via ξ_r only on the geometric standard deviation, S_r. The corresponding plot of the deviation factor (5.2) is depicted in Figure 5.2 for different values of the Poisson index χ.

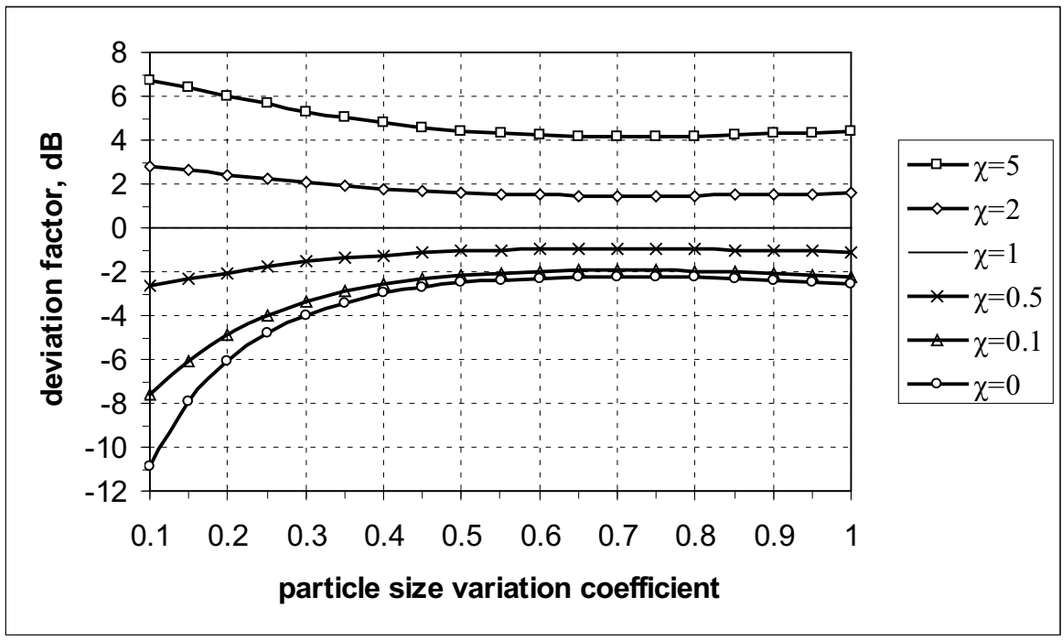

Fig.5.2. Deviation factor versus particle radius variation coefficient for different deviations of Poisson index χ from the Poisson law

As can be concluded from analysis of the plot, the deviation of ~12 dB emphasized in the previous section can be explained by the homogeneous microstructure of the dry snow zone, with approximately identical particle sizes (ξ_r<0.1) and negligible variations of the particle concentration (χ<<1) within the scattering volume. As an example of data supporting the current considerations, the results of comparative measurements of C-band backscatter from firn and in *situ* measurements of statistical parameters of firn dielectric permittivity for a study area in Antarctic (Zahnen et al., 2002) can be taken into account. In this study, dielectric permittivity was considered to be a measure of the heterogeneity of the snow/firn pack. A notable positive correlation was observed between backscattering signal strength and the standard deviation of the dielectric constant collected along 4 and 15 meters depth interval of several drills within a dry firn area. At the same time, a negative correlation takes place for a mean dielectric constant. Because the dielectric constant is

approximately linearly proportional to the density of dry snow (e.g., Tiuri et al., 1984), and therefore linearly proportional to the number of ice particles per unit volume as well, these correlations match the behavior of the deviation factor (5.2) on the Poisson index. The index and, hence, scattering increase with increasing variations in particle number and decrease with increasing $\langle n \rangle$. Of course, more comprehensive field data are needed to confirm this hypothesis.

The considerations provided above are related to the simplest case of complete burial of the probing pulse into a snow slab in the beamwidth-limited mode. Obviously, that the result is still the same for incomplete burial of the radial size of the scattering volume. The transverse size change of a slice within the scattering volume in the depth-limited mode results in an additional gradient in particle number among slices, and the contribution of this additional gradient to the backscatter should be analyzed in the future.

6. Normalized snow depth

6.1. Derivation of the normalized snow depth from the backscatter coefficient based on the enhanced semi-empirical model

After enhancing the semi-empirical model by the "slice" approach, one resume assessment of the snow depth, the key parameter in all mass-balance studies. To derive this parameter, let us to write down the enhanced semi-empirical model (ESEM) in a form more fitting for the Greenland ice sheet:

$$\sigma_t^0 = \sigma_s^0 + \sigma_i^0 = \sigma_v \frac{1}{2} L_p \cos\theta \left[1 - \exp\left(-2 \frac{h_\theta}{L_p} \right) \right] Y + \sigma_{i,\max}^0 \exp\left(-2 \frac{h_\theta}{L_p} \right) \tag{6.1}$$

where σ_i^0 is the backscatter coefficient from the ice layer, L_p is the penetration path (2.18), Y is the deviation factor (5.2), and $h_\theta = \frac{h}{\cos\theta}$ is the slant snow depth. Let us also denote: $\sigma_v \cdot \frac{L_p}{2} \cos\theta = \sigma_\infty^0$ as the saturation backscatter coefficient. Given these expressions, the normalized Snow Depth ($nSD = \frac{h}{L_p}$, see (3.25)) as a function of distance S along snow cover with a variable snow depth, h, can be derived from (6.1) to take the form:

$$nSD(S) = \frac{h(S)}{L_p} = -\frac{1}{2} \cos\theta(S) \cdot \ln \frac{\left[1 - \frac{\sigma(S)}{Y\sigma_\infty} \right]}{\left[1 - \frac{\sigma_i}{Y\sigma_\infty} \right]} \tag{6.2}$$

Here, $\sigma(S) \equiv \sigma_t^0(S)$, $\sigma_\infty^0 \equiv \sigma_\infty$ and $\sigma_i^0 \equiv \sigma_i$ to simplify the notation. If $Y \cdot \sigma_\infty >> \sigma_i$ then

$$nSD(S) = -\frac{1}{2}\cos\theta(S)\cdot\ln\left[1-\frac{\sigma(S)}{Y\cdot\sigma_{\infty}}\right] \tag{6.3}$$

The equation above indicates that the estimated normalized snow depth depends on number and kind of scatterers (σ_{∞}) and their statistical characteristics (Y) at small (less then wavelength) scales. Thus, to extract the *nSD* from measured radar data, $\sigma(S)$, one needs to know the product of the deviation factor and the saturation coefficient. To find the physical snow depth, the penetration path must also be known. It should

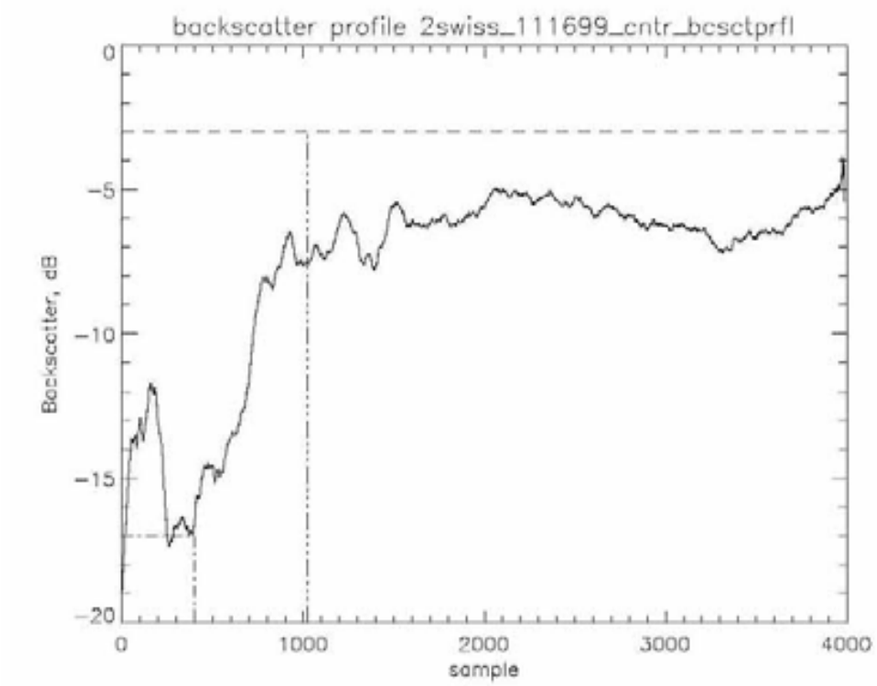

Fig.6.1. Typical backscatter coefficient profile across a transect within the margin of the Greenland Ice Sheet (in the vicinity of the Swiss camp)

be underlined, additionally, that the nSD $\left(=\frac{h}{L_p}\right)$ is not quite the same as the snow optical thickness $\left(=\frac{1}{L_p}\frac{h}{\cos\theta}=\frac{h_\theta}{L_p}\right)$. Obviously, $\tau_\theta \geq nSD$. nSD is a combination of the electromagnetic wave direction (L_p) and vertical geometrical (h) scaling factors of the snow depth. These two terms coincide only for sounding in the nadir direction.

From the point of view of practical measurements, detailed analysis recommends stopping the *nSD* estimate at a distance when $\left(\frac{\sigma(S)}{Y\cdot\sigma_{\infty}}\right)_{dB} \leq -2dB$. It should also be noted also that the deviation factor (Y) might be less or more than unit (Figure 5.2). Because the product $Y\cdot\sigma_{\infty}$ is generally unknown, it is reasonable to establish its value as ~2 dB higher than the value of

the backscatter profile plateau shown, for instance, in Figure 6.1. The backscatter profile has the main features inherent to the theoretical profile in the linear approach, as shown in Figure 3.3.

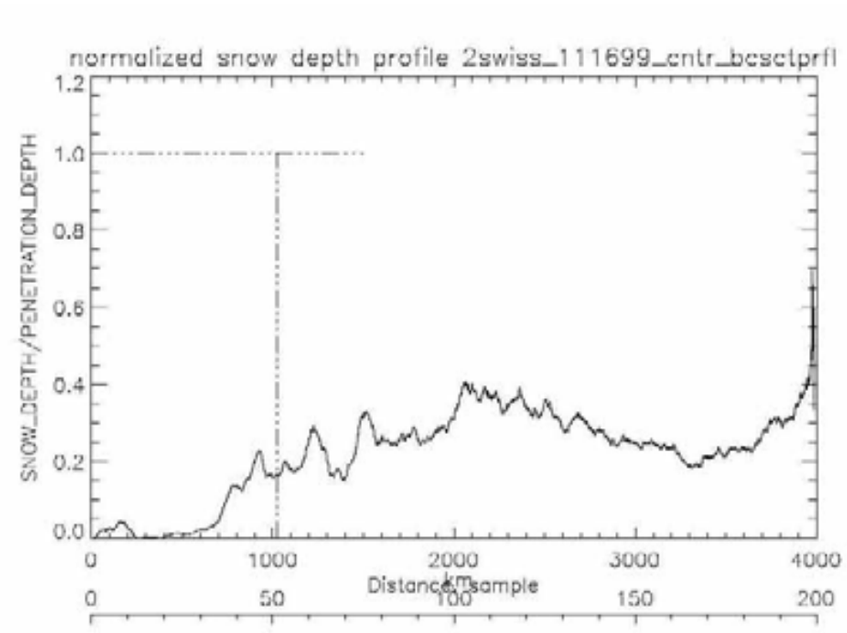

Fig. 6.2. The normalized snow depth profile derived from the backscatter coefficient profile in Figure 6.1

The profile has an exponential-like increase at the beginning of transect that transitions into a plateau-like, approximately constant level. Most probably, this level represents the saturation level caused by thick snow of depth greater than the propagation depth. The corresponding nSD is shown in Figure 6.2.

The nSD profile plotted in Figure 6.2 is obtained under the assumption that the deviation factor and the extinction coefficient are constant across the entire profile distance. Although the approach demonstrated here does not give the absolute value of the snow depth without certain assumptions, its advantage is that the assumptions are clearly delineated and put forth. In turn, if one has a calibration point (spot), the technique allows extension of the remote sensing methodology on vast remote areas with similar electromagnetic properties. In addition, the nSD is a relative indicator of the snow environment stability and redistribution.

The nSD in form (6.3) is derived from the ESEM, which in turn is based on consideration of a flat surface, plane wavefront and long probing pulse. Hence, the result obtained is most appropriate for SAR sounding of a thick snow slab.

6.2. An example of time transformation of nSD profiles within a selected Greenland marginal area

The normalized snow depth is sensitive to the geometrical snow depth and to the extinction coefficient. Assuming the snow microstructure to be homogeneous within a limited area, one can suppose that nSD depends only on the snow depth and thus apply nSD for snow

mass-balance assessment. An illustrative example of an nSD profile change after a 10-year period is shown in Figure 6.3.

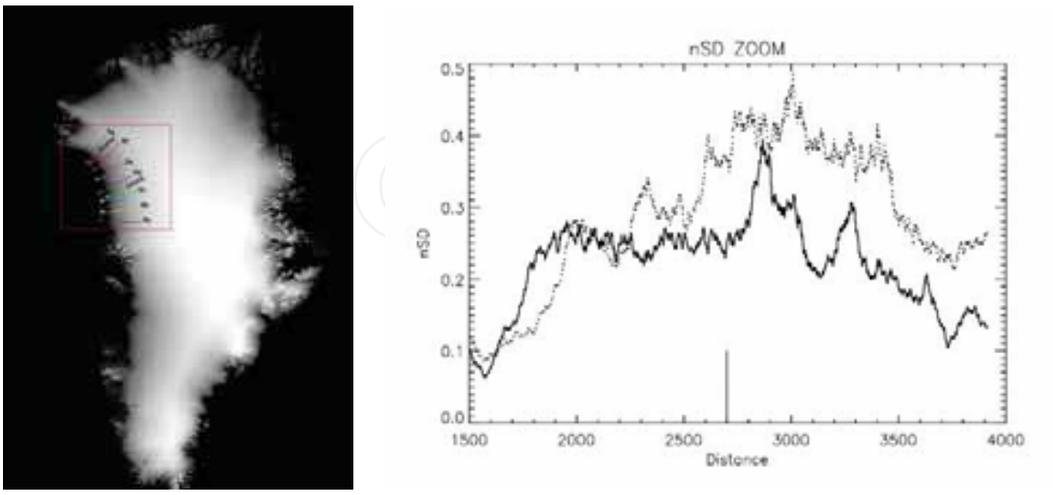

Fig.6.3. Study area #3 (box with center: 75.07^{0}N and 54.30^{0}W) within the Greenland ice sheet margin with several transects normal to the coastline (left). Normalized snow depth profiles (right) for transect 3a (lower line in the study area) derived from RadarSAT-1 data. Distance scale: 1 sample=50 m. Solid line is nSD profile on 11/16/1997, dotted line is nSD profile on 11/12/2007

The nSD profiles were derived from the RadarSAT-1 data archive from the Alaska Satellite Facility in Fairbanks (granules R1_10617_SWB_261 from 1997 and R1_62753_SWB_261 from 2007 with coordinates of the center scene 75.23^{0}N/54.29^{0}W and 75.22^{0}N/54.37^{0}W respectively, descending modes for both). As follows from the center locations of the data, the SAR shots were performed from practically the same point in the orbit and thus can be analyzed in parallel without additional corrections.

A comparative assessment of the nSD profiles indicates notable differences between the profiles. Generally, these changes can be caused snow mass redistribution within the 10-year period, variation of the extinction coefficient due to possible snow metamorphism, or both factors simultaneously. The detailed analysis of these factors and their "weights" in the deviations of these profiles is beyond the scope of this work but is planning for further consideration.

7. Model spectral dependence of the backscatter

7.1. Spectral dependence of the backscatter in accordance with the A-U model

The spectral (frequency) dependence of the backscatter coefficient within the framework of the semi-empirical model (A-U and ESEM) is the topic of the current section. The aim of this discussion is to find out how spectral features depend on the thick snow properties. Particularly, Davis & Moore (1993), namely assumed that a two-frequency radar system can provide quantitative estimates of snow physical properties.

The model consists of two components that are definitely frequency-dependent: the specific volume component (4.2) and the normalized effective depth of sounding (3.19).

Transforming the wavelength (λ) into the frequency $\left(F = \frac{c}{\lambda} \right)$, the combination of these two components gives, for the "intermediate" snow regime:

$$\sigma_s^0 = \left\{ Y \frac{Z_s}{c^4} F^4 h \right\} \left\{ \frac{L_p(F)\cos\theta}{2h} \left[1 - \exp\left(- \frac{2h}{L_p(F)\cos\theta} \right) \right] \right\} \tag{7.1}$$

The frequency-dependent core of (7.1) is

$$A(F, h_\theta) = 2 \frac{1}{Z_s} \frac{\sigma_s^0}{Y \cdot \cos\theta} = \left\{ \left(\frac{F}{c} \right)^4 \right\} \left\{ L_p(F) \left[1 - \exp\left(- \frac{2h_\theta}{L_p(F)} \right) \right] \right\} \tag{7.2}$$

where $h_\theta = \frac{h}{\cos\theta}$ is the slant snow depth; $L_p(F) = k_e(F)^{-1}$. The dimension of function (7.2) is [L^{-3}].

7.2. Estimation of spectral differences based on field penetration depth data

For further analysis, it is convenient to deal with the dimensionless spectral function, which can be obtained by multiplying the spectral core (7.2) by the cube of the wavelength:

$$B(F, h_\theta) = \lambda^3 A(F, h_\theta) = \left\{ \frac{F}{c} \right\} \left\{ L_p(F) \left[1 - \exp\left(- \frac{2h_\theta}{L_p(F)} \right) \right] \right\} \tag{7.3}$$

To evaluate (7.3) the spectral dependence of the penetration path (depth) should be estimated. One can state that the high frequency irradiance interacts primarily with the surface layer of snow with the relative small particles. And the low frequency irradiance penetrates deeper and, thus, is affected by particles which sizes are larger in accordance with the grain growth model (e.g., 4.18). For example, the grain radius changes from 0.25 to 0.6 mm within the depth of 10 m is in model of Drinkwater et al., (2001). In model of Forster et al., (1999) the range of the particles' changes is even more (up to 1 mm) and additionally depends on the accumulation rate. Thus, to get more realistic spectral dependence, we should take into account the depth of penetration of the electromagnetic wave into the snow and the corresponding grain size change within this depth. Therefore, there is an obvious paradox: to calculate frequency dependence of the penetration depth we should know the latter a priory. Moreover, due to chain: "frequency-penetration depth-particle size" the mean particle radius impacted the radar irradiance turns out to be dependent on the irradiance frequency. In additional, the A-U model was derived assuming the constant extinction coefficient, as it was mentioned in section 3. The solution of these questions should be evaluated in further research. Taking in mind the restrictions listed above, the penetration depth is assumed to be dependent only on frequency in the following estimation. Since the significance of the particles' size change compared with the fixed

mean size in the extinction coefficient calculation is currently unclear, it is reasonable to take the field data available in the literature (Table 7.1) for rough assessment the spectral dependence of the penetration depth.

#	Frequency, GHz	Penetration depth, m	Literature source
1	5 10 20 35	18 9 4.3 1.5	Hofer & Matzler, 1980
2	5 10 20 35	20 10 4.8 1.4	Matzler, 1987
3	5.2 6.6 10.3 10.7 18.0 37	21.7 17.8 8.1 10.4 3.2 0.85	Rott et al., 1993
4	10	3.4±1.3	Devis & Poznyak, 1993
5	13.5	3.5±1.5	Davis, 1996
6	5.3	27±4	Hoen & Zebker, 2000

Table 7.1. Literature data on the experimental penetration path (depth)

These field data can be approximated by a simple empirical power function

$$L_p \approx 223.44F^{-1.44} \tag{7.4}$$

with the coefficient of determination equals to 0.9. In (7.4) the penetration path is in meters and frequency is in GHz. It should be noted that field data, provided in the first three rows of Table 7.1, are obtained based on measurements within the surface layer of the snow (up to 3 m). It means that these data also do not take into account adequately the actual stratification of the thick dry snow cover of the Greenland ice sheet and, therefore, the further estimation should be considered only as a first approximation. A plot of (7.3) is shown in Figure 7.1. This plot demonstrates a notable discrimination in behavior of the spectral function $B(F,h_\theta)$ for different snow depths. Particularly, the magnitudes of the curves at a frequency of 5 GHz are notably different. Differences of the backscatter magnitude for frequencies of 5 and 14 GHz as a function of the slant snow depth are depicted in Figure 7.2.

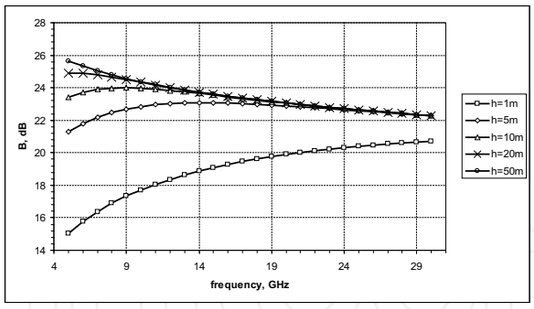

Fig. 7.1. Dimensionless spectral characteristics of the backscatter for several values of the slant snow depth based on the empirical spectral dependence of the penetration depth

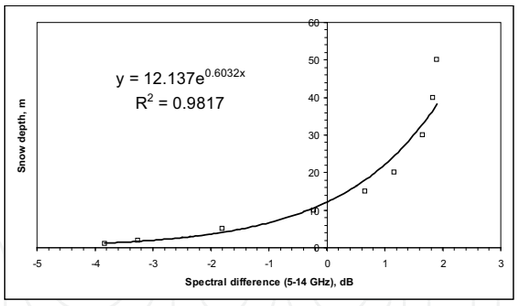

Fig. 7.2. Slant snow depth as a function of the magnitude difference between the dimensionless spectral components of the backscatter coefficients at 5 and 14 GHz

As follows from the approximation results,

$$h_\theta = 12.14 \cdot \exp(0.6 \cdot \Delta B_{5-14}) \tag{7.5}$$

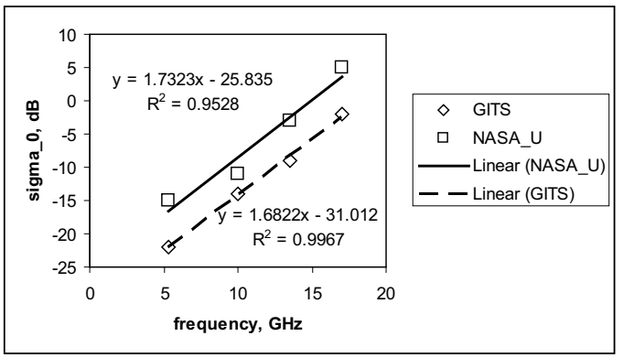

Fig. 7.3. Spectral pattern of the experimental data of (Baumgartner et al., 1999) for an incidence angle of 40^0 for two test sites in Greenland

where the slant snow depth is in meters and the spectral difference ΔB_{5-14} is in dB. An illustrative example of the spectral difference observed in Greenland can be provided from the known literature. Baumgartner at al. (1999) conducted field measurements of the backscatter coefficient from the dry snow site GITS (77.1^0N, 61^0W) and from the site NASA-U (73^0N, 50.5^0W) located between the dry snow and percolation zone for four wavelengths, 5.3, 10, 13.5 and 17 GHz, at temperature from -21^0C to -15^0C, with the ground-based radar. The primary goal of this experiment was to study the angular dependence of the backscatter. For our purposes, the spectral dependence related to the incidence angle of 40^0 (where the backscatter is expected to be due mainly to the volume scattering) can be extracted for the four points and is shown in Figure 7.3. Taking into account that $B(F, h_\theta) = \mu \frac{\sigma_s^0}{F^3}$, where μ is an unknown coefficient that we assume to be the same for all wavelengths, one can obtain the spectral ratio or the spectral difference in the logarithmic units for a pair of frequencies F_1 and F_2:

$$\Delta B_{dB,\,F_1-F_2} = B(F_1)_{dB} - B(F_2)_{dB} = \left[\sigma_s^0(F_1)_{dB} - \sigma_s^0(F_2)_{dB}\right] - 30\left[\lg F_1 - \lg F_2\right] \tag{7.6}$$

If, for example, F_1=5 GHz and F_2=14 GHz, we get:

$$\Delta B_{dB,\,5-14} = \left[\sigma_s^0(5)_{dB} - \sigma_s^0(14)_{dB}\right] + 13.41 \tag{7.7}$$

Differences in the backscatter coefficients of these frequencies for both test sites are approximately the same and equal roughly to -13 dB, as shown in Figure 7.3. Assuming the backscatter error of ~±0.5 dB, the corresponding spectral difference (from 7.7) is approximately equal to 0.4±0.5 dB. In accordance with (7.5), the slant snow depth is ~6.7-20.8 m. Since these data are related to an incidence angle of 40^0, the estimate of actual snow depth is 5.1-15.9 m. This value is in accordance with a note in the paper that the depth of snow was ~7-8 meters for the NASA-U site, at least.

Thus, a rough assessment of the snow depth within several selected dry snow areas, based on the spectral dependence of the backscatter in the frames of the SEM (ESEM), gives results comparable with in-situ measurements.

7.3. Spectral characteristics of the penetration depth for model monodisperse cold snow

It is interesting to compare the empirical (7.4) and theoretical frequency dependence of the penetration path (depth). Calculation of the extinction coefficient has been completed in the same manner as in section 3, with the additional estimation of particle concentration n^0 (see (4.8)):

$$n^0 = f_v \cdot \left(\frac{4}{3}\pi\, r^3\right)^{-1} \tag{7.8}$$

where $f_v = \frac{\rho_s}{\rho_i}$ is the fractional volume of ice in snow (0.2-0.4), ρ_s and ρ_i are density of snow and ice, respectively. We also should demarcate the frequency and particle size inherent to the Rayleigh approach ($2\pi r \frac{F}{c}|\dot{m}| \le 0.5$). The penetration depth (path) in snow is calculated for several combinations of snow density and particle size for a temperature of -15^0C. The result of this calculation is shown in Figure 7.4 together with the empirical dependence (7.4). The gently sloping of the empirical curve compared with the theoretical ones indirectly support the idea, mentioned above, about the contribution of the particle size in spectral behavior of the penetration depth (see the corresponded comments in the previous subsection).

In Figure 7.5, the results obtained from these calculations for T= -15^0C and the snow density of 0.3 g/m^3 are compared with the known values (Ulaby et al., 1986, Fig. 19.64, p.1608) for T= -1^0C and density of 0.24 g/m^3. The plot indicates the increasing of the penetration depth at low temperatures for the low frequency region, a trend most obvious for small particles of 0.5 mm radius. This behavior is explainable because the losses in snow caused by absorption decrease as the temperature decreases (Ulaby et al., 1986, Fig.E.3, p. 2027), and the absorption mechanism prevails over scattering in the low frequency region. Pointed changes become more apparent for small particles due to more significant role absorption plays for them as compared with large particles.

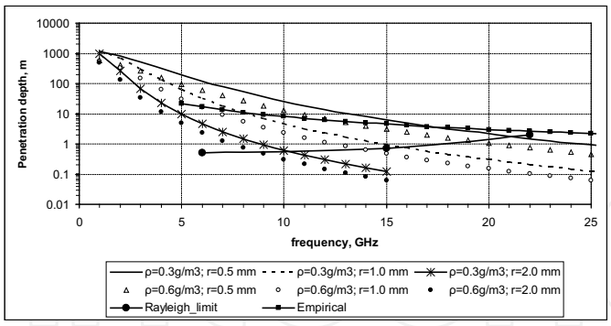

Fig.7.4. Theoretical spectral dependence under the Rayleigh approach of the penetration depth for a temperature of -15^{0}C (our calculations) with comparison of the empirical relationship (7.4)

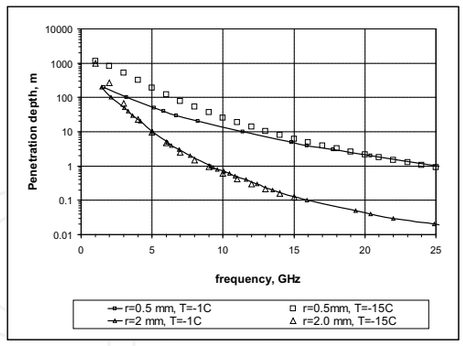

Fig.7.5. Comparison of the spectral dependence of the penetration depth calculated with Mie formulas for a temperature of -1^{0}C (Ulaby et al., 1986) with our calculations under the Rayleigh approach for a temperature of -15^{0}C

8. Backscatter depth profile model for snow sounding with broadband pulses of short effective (compressed) length

8.1. Phenomenological approach in the case of very short probing pulse

The above considerations apply when the scattering volume was less then the probing pulse volume. In the case of altimeter sounding of thick snow cover with short broadband chirp pulses this condition is not satisfied, the backscatter coefficient is represented not by the point of a radar signature but in the form of a backscatter profile along the wave propagation path. When $h_{sct}^{(p)} << h_\theta$ and $h_{sct}^{(p)} << L_p$, the volume component of the total backscatter from a snow area with the center located at a slant distance of R beneath the surface should simply mirror the backscatter coefficient depth distribution taking attenuation into account:

$$\sigma_s^0(R) = \frac{\sigma_s(R)}{A_{ill}} \exp(-2k_e R) \tag{8.1}$$

where $\sigma_s(R) = \sum_{i=1}^{N} \sigma_i$ is the total radar cross-section (RCS) of N scatterers contributing backscatter from a scattering volume V_{sct} from a distance R. Since the scattering volume is $V_{sct} = h_{sct}^{(p)} A_{ill} \cos\theta$, and taking the correction on the deviation factor into account (see section 5), the equation (8.1) can be presented in the form:

$$\sigma_s^0(R) = Y(R) \frac{\sigma_v(R)}{A_{ill}} V_{sct} \exp(-2k_e R) = Y(R) \sigma_v(R) h_{sct}^{(p)} \cos\theta \exp\left(-2\frac{R}{L_p(R)}\right) \tag{8.2}$$

where $\sigma_v = \frac{\sigma_s}{V_p}$ is the specific volume backscatter, and the return signal is proportional to the cosine of the incidence angle and has the envelope of the exponential form distorted by the variability of the statistical, scattering and absorption properties of the snow medium along the wave propagation path. The illuminated area A_{ill} (transverse size of the scattering volume) changes during the burial of the probing pulse into the snow slab due (mainly) to the wave sphericity in the depth-limited mode (see section 2). However, this effect does not impact the accuracy of the specific volume backscatter coefficient presented here, due to its the mutual cancellation in the nominator (via V_{sct}) and the denominator of equation (8.2). As a result of this cancellation, for very short probing pulses, the backscatter envelope depends only on changes in the specific volume backscatter with distance.

8.2. Analytical derivation for commensurate length of the scattering volume and snow depth

In general case, when $h_{sct}^{(p)} \sim \frac{h}{\cos\theta}$ and $h_{sct}^{(p)} \sim L_p$, the interactions between a probing pulse with a normalized form $U(R)$ and an extended target such as snow cover is described by the convolution integral (Moore & Williams, 1957):

$$P_r(t) = P_T(t) \otimes P_s(t) \tag{8.3}$$

where $P_r(t)$ is the return signal, $P_T(t)$ is the transmitted pulse profile and $P_s(t)$ is a term that includes the distribution range of the scattering facets, their scattering properties and the effects of the antenna gain. As applied our consideration of volume backscatter, one can write

$$\sigma_s^0(R) = \cos\theta \int_0^\infty dx \cdot U(x-R) \cdot Y(x)\sigma_v(x) \exp\left(-2\frac{x}{L_p(x)}\right) \tag{8.4}$$

If, for example, the probing pulse has a Gaussian form, which is usually an adequate approximation for short pulse systems (e.g., Brown, 1977), the weighting function of the scattering volume is $U(R) = \exp\left(-\beta\frac{R^2}{\Delta_q^2}\right)$, where Δ_q is the spatial duration of the scattering volume weight function at level $q = \exp\left(-\frac{\beta}{4}\right)$. For level q=0.5 (-3 dB), β=-4ln0.5=2.8. If, in addition, the microstructural, statistical and attenuation properties of the snow slab do not change along the propagation path within the snow pack, one can write:

$$\sigma_s^0(R) = \cos\theta \cdot Y\sigma_v \int_0^\infty dx \cdot U(x-R) \cdot \exp\left(-2\frac{x}{L_p}\right) \tag{8.5}$$

For short pulses, if their envelope can be represented by the delta-function, i.e., $U(x-R) \sim \delta(x-R)$, equation (8.5) yields the corresponding result obtained earlier (8.3) for the very short pulses configuration. For the long pulses, where $h_{sct}^{(p)} > L_p$ and $\sigma_s^0 \sim \int_0^L dx \exp\left(-2\frac{x}{L_p}\right)$, which yields to the standard form of the A-U model (3.13). For the general case, a closed-form solution of the equation (8.5) can be obtained.
Taking into account the tabulated integral (Abramowitz & Stegun, 1972):

$$\int_0^\infty dx \exp\left(-ax^2 - bx\right) = e^{\frac{b^2}{4a}} \frac{\sqrt{\pi}}{2\sqrt{a}} \Phi\left(\frac{b+2ax}{2\sqrt{a}}\right)\Bigg|_0^\infty = \frac{1}{2} e^{\frac{b^2}{4a}} \sqrt{\frac{\pi}{a}}\left[1 - \Phi\left(\frac{b}{2\sqrt{a}}\right)\right] \tag{8.6}$$

where $\Phi(x) = \frac{2}{\sqrt{\pi}} \int_0^x \exp\left(-t^2\right) dt$ is the error function, one can get the integral of equation (8.5) for a Gaussian probing pulse:

$$\int_0^\infty dx \cdot U(x-R) \cdot \exp\left(-2\frac{x}{L_p}\right) = \frac{1}{2}\Delta_q \sqrt{\frac{\pi}{\beta}} \exp\left[\frac{1}{\beta}\left(\frac{\Delta_q}{L_p}\right)^2 - 2\frac{R}{D_p}\right] \cdot \left[1 - \Phi\left(\frac{1}{\sqrt{\beta}}\left(\frac{\Delta_q}{L_p} - \frac{\beta}{\Delta_q} R\right)\right)\right] \tag{8.7}$$

If one denotes $\frac{\Delta_q}{\sqrt{\beta}} = \Delta$, then (8.5) has the form:

$$\sigma_s^0(R) = \cos\theta \cdot Y \sigma_v \Delta \frac{\sqrt{\pi}}{2} \exp\left[\left(\frac{\Delta}{L_p}\right)^2 - \frac{2}{L_p} R\right] \cdot \left[1 - \Phi\left(\frac{\Delta}{L_p} - \frac{1}{\Delta} R\right)\right] \tag{8.8}$$

Finally, if one denotes: $\sigma_{\max}^* = \frac{1}{2}\sigma_v L_p \cos\theta$ (see 3.24), $\left(\frac{\Delta}{L_p}\right) = \gamma$ and $S = \frac{R}{L_p}$, the closed-form solution of equation (8.6) using these dimensionless parameters can be written as:

$$\sigma_s^0(S) = Y \sigma_{\max}^* \sqrt{\pi}\gamma \exp\left(\gamma^2 - 2S\right) \cdot \left[1 - \Phi\left(\gamma - \frac{S}{\gamma}\right)\right] \tag{8.9}$$

Distance normalization in (8.9) is chosen through the parameter *S* for the purpose of comparing the backscatter profile calculated here with the modeled "clear" backscatter profile derived for a very short pulse (8.2) and governed only by attenuation. The equation obtained is close to the volume component of the SV model of Davis & Moore (1993). The

distinctions of the current approach are that it uses a slightly different description of the pulse-snow interaction, the end result is written in terms of the backscatter coefficient depth profile, and the state of homogeneity of the snow mass is taken into account through the deviation factor, *Y*. It is interesting, that equation (8.9) coincides with the backscatter model from the sea surface, obtained by Barrick (1972), exactly by the form with, of course, other meaning of model parameters.

8.3. Comparison of the results obtained with the phenomenological approach

8.3.1. Very short probing pulse

For the limit case when $\gamma << 1$, and taking into account that $\Phi(-x) = -\Phi(x)$ and $\lim_{x\to\infty} \Phi(x) = 1$ (Abramowitz & Stegun, 1972), the corresponding backscatter coefficient is:

$$\sigma_s^0(S)_{\gamma<<1} = Y\sigma_{\max}^* \sqrt{\pi}\gamma \exp[-2S]\cdot\left[1-\Phi\left(-\frac{1}{\gamma}S\right)\right] = Y\sigma_{\max}^* \sqrt{\pi}\gamma \exp[-2S]\cdot\left[1+\Phi\left(\frac{1}{\gamma}S\right)\right] \approx \quad (8.10)$$

$$2Y\sigma_{\max}^* \sqrt{\pi}\gamma \exp(-2S) = \cos\theta\, Y\sigma_v \Delta\sqrt{\pi}\, \exp(-2S)$$

This result confirms relationship (8.2) obtained above based on phenomenological considerations.

8.3.2. Long probing pulse

Taking into account the asymptotic value of the error function $\Phi(x) \underset{x>>1}{\approx} 1 - e^{-x^2}\frac{1}{\sqrt{\pi}x}\left(1-\frac{1}{2x^2}-...\right)$ (Abramowitz & Stegun, 1972), and taking only the first term of the extension, we get the value of (8.9) for γ>>1:

$$\sigma_s^0(S)_{\gamma>>1} \approx Y\sigma_{\max}^* \sqrt{\pi}\gamma \exp(\gamma^2 - 2S)\exp\left[-\gamma^2 + 2S - \left(\frac{S}{\gamma}\right)^2\right]\frac{1}{\sqrt{\pi}}\left(\gamma - \frac{S}{\gamma}\right)^{-1} \quad (8.11)$$

For long pulses, the available distance variation is much less than the pulse length, i.e., $\left(\frac{S}{\gamma}\right)_{\gamma>>1} = \frac{R}{\Delta} << 1$. Hence,

$$\sigma_s^0(S)_{\gamma>>1} \approx Y\sigma_{\max}^* \exp\left[-\left(\frac{S}{\gamma}\right)^2\right]\left(1-\frac{S}{\gamma^2}\right)_{\gamma>>1}^{-1} \approx Y\sigma_{\max}^* = \frac{1}{2}\cdot Y\sigma_v D_p^* \quad (8.12)$$

This expression also confirms the result of the A-U model (enhanced) under thick snow condition (3.24). Thus, an important positive feature of the model (8.9) is that its results coincide with those obtained with phenomenological approaches for extreme values of the scattering volume (much less and much more than the penetration path respectively).

Nevertheless, it should be noted that ignoring the change in the illumination area during the burial of the probing pulse into snow media is, strictly speaking, valid only for a short probing pulse or for the beamwidth-limited mode. For long and intermediate-length probing pulses with wavefront sphericity in the commonly-existing depth-limited configuration, this effect should be taken into account because there are slices (see sections 2 and 5) of different transverse sizes within $h_{sct}^{(p)}$.

8.4. Numerical calculation of the return signal for intermediate length of the probing pulse

A plot of the normalized backscatter coefficient $\sigma^*(S,\gamma)=\frac{\sigma_s^0(S,\gamma)}{\sigma_s^0(S_{\max},\gamma)}$ ($S_{\max}$ is the normalized distance where function (8.7) has the maximum value at a given γ) is shown in Figure 8.1.

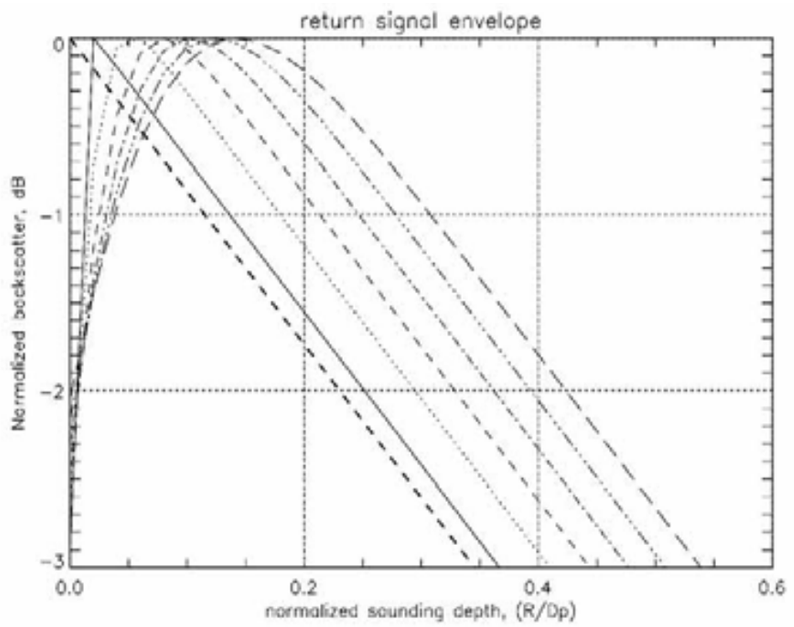

Fig.8.1. Illustration of the reproducibility of the snow backscatter uniform profile taking into account only attenuation (bold dash line) and finite probing pulse length normalized to the penetration depth (parameter $\gamma = \Delta / L_p$).

Legend: solid line, γ=0.01; dot line, γ=0.035; dashed line, γ=0.06; dashed-dot line, γ=0.085; dashed-dot-dot line, γ=0.11; long dashed line, γ=0.135

This figure illustrates the contribution of the pulse length to the return signal envelope pattern. The shorter pulse clearly gives a better approximation of the real backscatter profile. Contemporary altimeters use a probing pulse with a physical duration of 20-50 microseconds and a corresponding effective duration (due to intrapulse frequency chirping) equal to 3.125 nanoseconds (e.g., Rosmorduc et al., 2006). In spatial units, these values are

equivalent to $\Delta \approx \frac{c\tau_0}{2} \approx 0.5$ m. For L_p~10-50 m, the expected values of the parameter γ range from 0.05 to 0.01. An important feature of this plot is that the value of the maximum of the return signal for any maximum position ($S_{\max}$) and values of parameter γ are the same:

$$\sigma_s^*\left(S_{\max},\gamma\right) = \sqrt{\pi}\sigma_{\max}^* Y \tag{8.13}$$

9. Summary

The semi-empirical model of the volumetric component of the backscatter coefficient, proposed by Attema & Ulaby (1978) (SEM or A-U model) is considered in more detail. The basic advantage of the SEM is its mathematical simplicity and clear physical sense but the SEM, derived using the incoherent approach, does not explain some remote sensing experimental data collected over the dry snow zone of the Greenland ice sheet. We discuss the main configurations of radar sounding of snow, including the relationships between the technical and positional parameters of radar on one hand and the geometrical and electromagnetic properties of snow cover on the other. Based on this consideration, the field of applicability of the SEM is figured out for the further assessments. Some qualitative assessments of the configuration of the scattering volume were carried out using plane and spherical surface approaches. More detailed study of the diffraction of space-bounded spherical electromagnetic wave on a large and strongly absorbing dielectric sphere with a rough surface is needed to evaluate this problem further. Detailed SEM estimates and experimental radar data over the dry snow zone of the Greenland ice sheet are provided for the negative temperatures inherent to the winter seasons. Data analysis shows a significant discrepancy between the expected and actually measured values of the backscatter coefficient. Possible reasons for the observed deviations of the SEM results are discussed based on the enhanced semi-empirical model (ESEM) and analysis of the dependence of the backscatter coefficient on the snow optical thickness and its spectral function. The ESEM is obtained on the basis of the so-called "slice" approach, taking into account partially-coherent backscattering due to finite wave front size and considering the contribution of the statistical characteristics of small-scale fluctuations of concentration and of sizes of the ice particles in a snow pack. The known semi-empirical model is only a special case of the ESEM. Using the ESEM, some observable radar signatures of the Greenland ice sheet, including the dry snow zone, can be interpreted in terms of the statistical characteristics of the snow microstructure. The model obtained retains the mathematical simplicity and physical clarity of the known A-U model and significantly expands its application for the interpretation of experimental data. Available field data, which confirm the consistency of the ESEM with observed values of the backscatter coefficient, are also provided. As a consequence of this analysis, the concept of the normalized snow depth (nSD) is formulated, and its practical application for monitoring snow mass displacement is described. The frequency-dependent core of the backscatter has been analyzed as well. Empirical and theoretical spectral characteristics of the penetration depth are also presented. The result allow for improvements in our understanding of opportunities for a two-frequency method of sounding thick snow covers and promote more accurate interpretations of the known experimental data. The extension of the ESEM for sounding thick snow cover with broadband pulses of short effective length

is also discussed, resulting in an exact description of the return signal envelope as a function of the electromagnetic and microstructural characteristics of the snow cover. The validity of the model is supported by the coincidence of the model estimates with assessments obtained for several specific cases using phenomenological approach. In conclusion, this work demonstrates that the enhanced version of the semi-empirical model can be applied successfully in the analysis of radar backscatter from thick snow cover.

10. Acknowledgements

This work was supported by NASA's Cryospheric Sciences Program. The author would like to thank Dr. W. Abdalati for his permanent attention to this work and useful discussions.

11. References

Abramowitz, M., & I.A. Stegun, Eds. (1972). Hanbook of mathematical functions with formulas, graphs, and mathematical tables. New York: Wiley.

Alley, R.B., Bolzan, J.F., & Whillans, I.M. (1982). Polar firn densification and grain growth. Ann Glaciol., vol.3, pp.7-11.

Atlas, D. (1964). Advances in radar meteorology. Advances in Geophysics, vol.10, pp. 317-479.

Attema, E., & Ulaby, F. (1978). Vegetation modeled as water cloud. Radio Science, vol.13, pp. 357-364.

Barrick, D. E. (1972). Remote sensing of sea by radar. In Derr, V. ed. Remote sensing of the troposphere. Washington, DC, U.S. Government Printing Office, pp. 12.1-12.46.

Battan, L.J. (1959). Radar Meteorology, Univ. of Chicago Press, Chicago, Ill.

Baumgarnter F., Jezek K., Forster R.R., Gogineni S.P., & Zabel I.H.H. (1999). Spectral and angular ground-based radar backscatter measurements of Greenland Snow facies. IGARSS'99 Proceedings, 28 June-2 July 1999, Humburg, vol.2, pp. 1053-1055.

Benson, C. S. (1996). Stratigraphic studies in the snow and firn of the Greenland ice sheet. U.S. Army Cold Reg. Res. and Eng. Lab (CRREL), Rep.70, 120 pp. Hanover, NH. (Revised edition of 1962 report).

Brown, G.S. (1977). The average impulse response of a rough surface and its applications. IEEE Transactions on Antennas and Propagation, vol. AP-25, No. 1, January 1977, pp. 67-74.

Clift, G.A. (1985). Use of radar in meteorology. Secretariat of the World Meteorological Organization, Geneva.

Davis, C.H. (1996). Temporal change in the extinction coefficient of snow on the Greenland Ice sheet from an analysis of Seasat and Geosat altimeter data. IEEE Trans. Geosci. Remote Sens., vol.34, No.5, September 1996, pp. 1066-1073.

Davis C.H., & Pozdnyak V.I. (1993). The depth of penetration in Antarctic firn at 10 GHz. IEEE Trans. Geosci. Remote Sens., vol. 31, No.5, September 1977, pp. 1107-1111.

Davis, C.H., & Moore, R.K. (1993). A combined surface- and volume scattering model for ice-sheet radar altimeter. Journal of Glaciology, vol. 39, No. 133, pp. 675-686.

Drinkwater M.D., Long D.G., & Bingham A.W. (2001). Greenland snow accumulation estimates from satellite radar scatterometer data. Journal of Geophysical Research, vol. 106, No. D24, December 2001, pp. 33,935-33,950.

ERS-1 and ERS-2 SAR Images. ASF document. September 18, 1996, 21 p. Available online: http://www.asf/alaska.edu/content/reference/pdf/ERSproducts.pdf

Etheridge D.M., Steele L.P., Francey R.J., & Langenfelds R.L. (2001). Historic CH_4 records from Antarctic and Greenland ice cores, Antarctic firn data, and archived air samples from Cape Grim, Tasmania. Available online: http://ediac.ornl.gov/trends/atm_meth/lawdome_meth.html

Fabelinskii I. L. (1968). Molecular scattering of light. Translated from Russian, New York, Plenum Press.

Forster R.R., Jezek, K.C., Bolzan, J., Baumgartner, F., & Gogineni, S.P. (1999). Relationship between radar backscatter and accumulation rates on the Greenland ice sheet. Int. J. Remote Sensing, vol. 20, No. 15&16, pp. 3131-3147.

Fung A.K. (1994). Microwave Scattering and Emission Models and Their Applications. Boston, Artech House, Inc.

Gossard E.E., & Srauch, R.G. (1983). Radar observation of clear air and clouds. Elsevier, New York.

Higham, M., & Craven, M. (1997). Surface mass balance and snow surface properties from the Lambert Glacier Basin traverses 1990-94. Tech. Rep. Res Rep. 9, Antarctic CRC, Hobard, Australia.

Hoen E.W., & Zebker H.A. (2000). Penetration depths inferred from interferometric volume decorrelation observed over the Greenland Ice Sheet. IEEE Trans. Geosci. Remote Sens., vol.38, No.6, November 2000, pp. 2571-2583.

Hofer R., & Matzler C. (1980). Investigations of snow parameters by radiometry in the 3 to 60 mm wavelength region. Journal of Geophysical Research, vol. 85, pp. 453-460.

Jaedicke, C., T. K. Thiis & Bang, B. (2000). The snowdrift around a small hill in the High Arctic. Proceedings of the 4th Int. conference on Snow Engineering. Trondheim, Norway, 19-21 June 2000. Hjoth-Hansen, Holand, Loset & Norem (eds). Balkema, Rotterdam, pp. 75-80.

Jezek, K. C., P. Gogineni & Shanableh, M. (1994). Radar measurements of melt zones on the Greenland Ice Sheet. Geophysical Research Letters, vol. 21, No. 1, pp. 33-36.

Kendra J.R., K. Sarabandi, & Ulaby, F.T. (1998). Radar measurements of snow: experiment and analysis. IEEE Trans. Geosci. Remote Sens., vol. 36, No. 3, May 1998, pp. 864-879.

Koskinen J. (2001). Snow monitoring using microwave radars. Thesis for the degree of Doctor of Technology. Helsinki University of Technology, Espoo, January 2001, Report 44, 31p.

Liu, T.W. (2002). Progress in scatterometer application. Journal of Oceanography, vol. 58, pp. 121-136.

Lo, Y.T., & S.W. Lee, Eds. (1993). The antenna handbook. Volume II, Antenna theory. New York, Van Nostrand Reinhold.

Lytle, V.I., & Jezek, K. (1994). Dielectric permittivity and scattering measurements of Greenland firn at 26.5-40 GHz. IEEE Trans. Geosci. Remote Sens., vol. 32, March 1994, pp. 290-295.

Matzler, C. (1987). Application of Interaction of Microwaves with the natural snow cover. Remote Sensing Reviews, vol. 2, pp. 259-387.

Moore, R.K., & Williams, C.S. (1957). Radar terrain return at near vertical incidence. Proceedings Institute of Radio Engineers, vol. 45, pp. 228-238.

Naito, K., & Atlas, D. (1966). On microwave scatter by partially coherent clouds, In Proc. 12th Weather Radar Conf., AMS, Norman, OK, October 17-20, 1966, pp. 7-12.

Newkirk, M.H., & Brown, G.S. (1996). A waveform model for surface and volume scattering from ice and snow. IEEE Trans. Geosci. Remote Sens., vol. 34, No. 2, March 1996, pp. 444-456.

Newkirk, M.H., & Brown, G.S. (1992). Issues related to waveform computations for radar altimeter applications. IEEE Trans. Geosci. Remote Sens., vol. 40, No. 12, December 1992, pp. 1478-1488.

Noveltis, C.R. (2005). Feasibility study of imaging the Antarctic ice using a spaceborne P-band radar. WP 200: Electromagnetic Model Review Document, ESA Contract Number 18195/04/NL/CB, p. 91, 2005.

RadarSAT -1 Standard Beam SAR Images. ASF document. June 21, 1999, 20 p. Available online:
http://www.asf/alaska.edu/content/reference/pdf/R1stanprod.pdf

Rosmorduc, V., J.Benveniste, O. Lauret, M. Milagro, & Picot, N. (2006). Radar Altimetry Tutorial, J. Benveniste and N. Picot (Eds)., 301p. Available online: http//www.altimetry.info.

Rott H., Sturm K., & Miller H. (1993). Active and passive microwave signatures of Antarctic firn by means of field measurements and satellite data. Annals of Glaciology, vol. 17, pp. 337-343.

Schytt, V. (1964). Scientific results of the Swedish glaciological expedition to Nordaustlandet, Sptisbergen, 1957 and 1958. Geografiska Annaler, vol. 44, pp. 243-281.

Scott, J.B.T., Mair, D., Nienow, P., Parry, V., & Morris, E. (2006). A groud-based radar backscatter onvestigation in the percolation zone of the Greenland ice sheet. Remote Sensing of Environment, vol. 104, pp. 361-373.

Shi, J., R.E. Davis, & Dozier, J. (1993). Stereological determination of dry-snow parameters for discrete-scatterer microwave modeling. Ann. Glaciol., vol. 17, pp. 295-299.

Siegert A.J.F., & Goldstein, H. (1951). Coherent and incoherent scattering from assemblies of scatterers, /In: Propagation of short radio waves. D.E. Kerr, (Ed), McGraw-Hill, New York.

Tiuri, M.E., A.H. Sihvola, E.G.Nyfors, & Hallikainen, M.T. (1984). The complex dielectric constant of snow at microwave frequencies. IEEE Journal of Oceanic Engineering, vol. OE-9, No. 5, pp. 377-382, December 1984.

Tsang, L., J. Pan, D. Liang, Z. Li, D. W. Cline, & Tan, Y. (2007). Modeling active microwave remote sensing of snow using dense media radiative transfer (DRMT) theory with multiple-scattering effects. IEEE Trans. Geosci. Remote Sens.. vol. 45, No. 4, April 2007, pp. 990-1004.

Ulaby F.T., Moore R.K., & Fung A.D. (1982). Microwave Remote Sensing, Active and Passive. Vol. II. Radar Remote Sensing and Surface Scattering and Emission Theory. Artech House, Inc., Norwood.

Ulaby F.T., Moore R.K., & Fung A.D. (1986). Microwave Remote Sensing, Active and Passive. Vol. III. From Theory to Applications. Artech House, Inc., Norwood.

Ulaby, F.T. , P. Siqueira, A. Nashashibi, & Sarabandi, K. (1996). Semi-empirical model for radar backscatter from snow at 35 and 95 GHz. IEEE Trans. Geosci. Remote Sens., vol. 34, No. 5, pp. 1059-1065, September 1996.

Woods, G.A. (1994). Grain growth behavior of the GISP2 ice core from central Greenland. Technical Report Series 94-002, Earth System Science Center, Penn State University, USA.

Yurchak, B.S. (2009). Radar volume backscatter from spatially extended geophysical targets in a "slice" approach. IEEE Trans. Geosci. Remote Sens., vol. 47, issue 10, (in press).

Zahnen, N., F. Jung-Rothenhausler, H. Oerter, F. Wilhelms & Miller, H. (2002). Correlation between Antarctic dry snow properties and backscattering characteristics in Radarsat SAR imagery. Proceedings of EARSeL-LISSIG_Workshop Observing our Cryosphere from Space, Bern, March 11-13, 2002, pp. 140-148.

Zwally, H.J., & Brenner, A.C. (2001). Ice sheet dynamics and mass balance. In book: Satellite altimetry and earth sciences. L.L. Fu and A. Cazenave, (Eds). International Geophysics series, vol. 69, pp. 351-369.

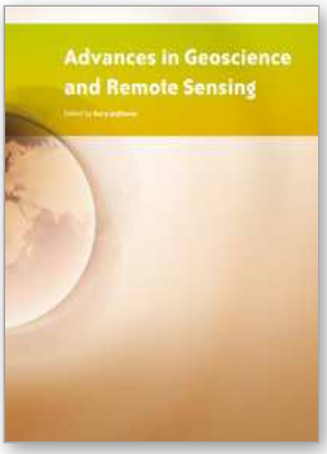

Advances in Geoscience and Remote Sensing

Edited by Gary Jedlovec

ISBN 978-953-307-005-6

Hard cover, 742 pages

Publisher InTech

Published online 01, October, 2009

Published in print edition October, 2009

Remote sensing is the acquisition of information of an object or phenomenon, by the use of either recording or real-time sensing device(s), that is not in physical or intimate contact with the object (such as by way of aircraft, spacecraft, satellite, buoy, or ship). In practice, remote sensing is the stand-off collection through the use of a variety of devices for gathering information on a given object or area. Human existence is dependent on our ability to understand, utilize, manage and maintain the environment we live in - Geoscience is the science that seeks to achieve these goals. This book is a collection of contributions from world-class scientists, engineers and educators engaged in the fields of geoscience and remote sensing.

InTech Europe
University Campus STeP Ri
Slavka Krautzeka 83/A
51000 Rijeka, Croatia
Phone: +385 (51) 770 447
Fax: +385 (51) 686 166
www.intechopen.com

InTech China
Unit 405, Office Block, Hotel Equatorial Shanghai
No.65, Yan An Road (West), Shanghai, 200040, China
中国上海市延安西路65号上海国际贵都大饭店办公楼405单元
Phone: +86-21-62489820
Fax: +86-21-62489821

IntechOpen